Absolute Photon Flux Measurement at the BGO-OD-Experiment

Katrin Kohl

Masterarbeit in Physik
angefertigt im Physikalischen Institut

vorgelegt der
Mathematisch-Naturwissenschaftlichen Fakultät
der
Rheinischen Friedrich-Wilhelms-Universität
Bonn

September 2016

I hereby declare that this thesis was formulated by myself and that no sources or tools other than those cited were used.

Bonn, ...
Date Signature

1. Gutachter: Prof. Dr. Hartmut Schmieden
2. Gutachter: Priv.-Doz. Dr. Wolfgang Hillert

Acknowledgements

I would like to thank all who supported me during my thesis. I would like to thank Prof. Schmieden for giving me an interesting topic with aspects from hardware and analysis. I would like to thank Priv. Doz. W. Hillert for beeing my evaluator for this thesis.
I would also like to thank Dr. Tom Jude for taking time of his busy schedule to read my thesis and giving me suggestions for improvements. I would like to thank Thomas Zimmermann for answering all my questions and helping me solve many problems. I would like to thank Dr. Jürgen Hannappel for his support in all technical questions. Furthermore I would like to thank the whole working group for being open for questions all the time and making this year a great experience for me.

Contents

1 Introduction 1

2 The BGO-OD Experiment 3
- 2.1 ELSA . . . 3
- 2.2 The BGO-OD Experiment . . . 4
- 2.3 Tagger . . . 5
- 2.4 GIM and FluMo . . . 7
  - 2.4.1 GIM . . . 7
  - 2.4.2 FluMo . . . 7

3 Photon Efficiency 9

4 Determination of the tagging efficiency P_γ 15
- 4.1 P_γ from experimental data . . . 15
- 4.2 Simulation of P_γ . . . 18
- 4.3 Optimization of P_γ . . . 22

5 $\gamma p \rightarrow \pi^0 p$ Cross Section 27
- 5.1 Cross Section Formula . . . 28
  - 5.1.1 $\pi^0 p$ reconstruction . . . 28
  - 5.1.2 Detection Efficiency . . . 29
  - 5.1.3 Photon Flux . . . 30
- 5.2 Results . . . 32

6 Summary and Conclusion 35

Bibliography 37

A Appendix 39
- A.1 $\pi^0 p$ cross section . . . 39

List of Figures 43

CHAPTER 1

Introduction

For thousands of years scientists are curiously searching for the smallest structures in our universe. What the ancient Greeks called *atomos*, the unpartable, we know today is very well divisible. The atom in modern understanding is the smallest part of a chemical element, but has indeed a substructure. In 1911 Ernest Rutherford scattered alpha particles on gold atoms, intending to find out more about their structure. His findings indicated a small massive positively charged centre with a large empty space around it, where the negatively charged electrons are placed. This experiment used the concept of cross section, describing the probability of an interaction per interaction centre.
It took only eight years until it was discovered, that atomic nuclei have a substructure themselves and are by no means elementary particles. The charged particles that build the nuclei were called protons. In 1932 James Chadwick discovered a neutral particle, the neutron. Together proton and neutron form atomic nuclei and are thus called nucleons. We know today that nucleons consist of two different types of particles called up and down quark. Four more quarks were discovered and called charm, strange, top and bottom. These particles are confined by the strong force. They never exist alone, but form bound states called hadrons. They form not only the constituents of atomic nuclei, but many more states, that can be sorted in two groups depending on the combination of quarks. States formed by one quark and one anti-quark are called mesons, three-quark states are called baryons. [1]

The structure of such states is not fully understood, especially the spectrum and structure of excited states. One way to investigate this is the photo production of mesons off nucleons. This is the method used at the BGO-OD experiment. A bremsstrahlung photon beam hits a fixed target of nucleons, e.g. liquid hydrogen, and produces mesons in the process. Differential cross section measurements are an important constraint to understand the photo production process. The knowledge of the photon flux is a prerequisite to measure an absolute cross section, not because it affects the shape, but because it determines the value.
At the BGO-OD experiment the photon flux is determined in several steps. The photon beam is produced via bremsstrahlung and energy tagged by a magnetic spectrometer for bremsstrahlung electrons in the Tagger. This counts the number of bremsstrahlung photons, and basically would already give the absolute photon flux. As the beam is collimated the measurement becomes more complicated. A second detector, the Gamma Intensity Monitor (GIM), which is a total absorbing lead glass block, is placed in the photon beam behind the collimator to determine the tagging efficiency P_γ. The tagging efficiency describes the probability to see a photon when having counted an electron. For in-situ measurements this second detector is exposed to the full photon flux and thus limited by rate. Therefore, it is complemented by a detector counting only a fraction of the photons, which is called Flux Monitor or short FluMo. The

photon efficiency describes the fraction of photons that is counted by this third detector. This quantity has to be known very well to obtain the photon flux.

The goal of this thesis is to determine the photon flux at the BGO-OD experiment. This includes a hardware upgrade of the FluMo, a calibration of the photon efficiency, and the determination of the tagging efficiency. A cross check of the flux determination is obtained by measuring the well known cross section of π^0 photo-production. The thesis is organized as follows: In chapter 2 the experiment is introduced and the detectors are explained in as much detail as necessary to understand this thesis. The next chapter explains how the photon efficiency is determined and investigates its dependence of different parameters. In chapter 4 the tagging efficiency is determined. This is first done with experimental data in chapter 4.1. In a second step the expected tagging efficiency is simulated and compared to the real data (chapter 4.2). As this shows discrepancies the importance of a good collimator alignment will be discussed in 4.3. Finally the well known $\gamma p \rightarrow p\pi^0$ cross section is determined and compared to previous measurements in chapter 5.

CHAPTER 2

The BGO-OD Experiment

The BGO-OD experiment is an international project, located at the ELSA accelerator-facility at the University of Bonn. It uses a tagged bremsstrahlung photon beam incident on a fixed target to investigate the photo production of mesons off nucleons.

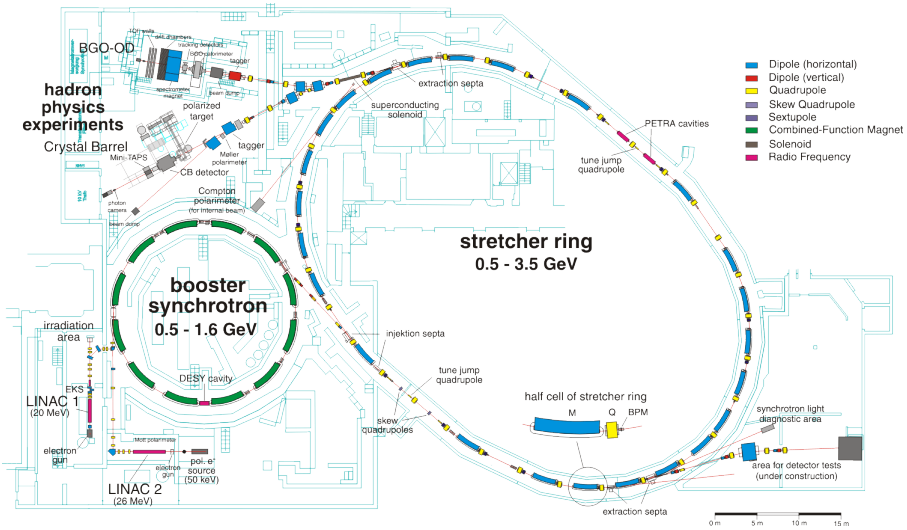

Figure 2.1: Overview of ELSA. The beam is produced in the lower left corner at the LinAcs, continues through booster synchrotron and stretcher ring to the experiments. The experimental areas are shown in the upper left corner.

2.1 ELSA

The ELSA accelerator-facility in Bonn was the first high duty-factor electron accelerator in the GeV-regime. As a University machine, students participate in design and operation. An overview of the accelerator is shown in figure 2.1. ELSA (Electron Stretcher Accelerator) accelerates polarized as well as unpolarized electrons up to a maximum energy of 3.5 GeV. Especially for polarization through coherent bremsstrahlung this is an interesting energy as high photon beam polarization can be obtained throughout the ideal energy regime for studying nucleon resonances. The acceleration is done in three steps: A linear accelerator gives the electrons an energy of about 20 MeV before they are injected into the booster

synchrotron. Here the electrons can be accelerated to an energy between 0.5 GeV and 1.6 GeV. From the booster synchrotron the electrons are fed into the stretcher synchrotron which also functions as a storage ring. The electrons are accelerated in high frequency cavities and by ramping the magnets up to higher fields a maximum energy of 3.5 GeV can be reached. In order to achieve a better duty-factor several pulses are accumulated in the ring and ramped together. With this setup a quasi continuous electron beam of more than 1 000 pA can be extracted to two experimental areas. One is used by the CB-ELSA/TAPS-Experiment. The other serves the BGO-OD experiment.[2]

2.2 The BGO-OD Experiment

The BGO-OD experiment consists of three main parts: The tagging system, the **BGO**-calorimeter and the **O**pen- **D**ipole forward spectrometer, shown in Fig. 2.2. The electron beam coming from the accelerator is converted to a real photon beam via bremsstrahlung and the energy is measured with the Tagger (see chapter 2.3). The photon beam is incident upon a fixed target, which is either liquid hydrogen, deuterium or solid targets such as carbon. The target is located in the center of the BGO-calorimeter. The calorimeter is made of 480 $Bi_4Ge_3O_{12}$ scintillator crystals with a length of 24 cm corresponding to approximately 21 radiation lengths. They are arranged in 15 sectors in θ [1], covering the angular range from 25° to 155°, leaving a gap around the beam-line. The incident particles deposit energy and excite the scintillator material. When the scintillator deexites it emits light. The light is read out via photomultiplier tubes (PMT). The calorimeter is optimized for photon and electron detection but also suited for low energetic hadrons. For charged particle identification a scintillator barrel, made of 32 scintillator strips, is located inside the BGO-calorimeter. Even further inside surrounding the target the calorimeter is supplemented by a cylindrical multi-wire proportional chamber (MWPC) for track reconstruction [3].

Downstream of the central detector, the θ angles smaller than 10° are covered by the forward spectrometer, consisting of an open dipole magnet and several tracking detectors. In front of the magnet the two scintillating fiber detectors MOMO and SciFi2 measure the position and direction of the particle [4]. The particle then proceeds through the magnetic field of the OD-magnet. Behind the magnet eight drift chambers measure the position and direction of the particle again [5]. The particle momentum is calculated from the curvature of the particle trajectory in the magnetic field according to:

$$p = mv = qBr, \tag{2.1}$$

where p is the momentum, m the mass, q the charge , r the radius of the curvature, v the velocity of the particle, B the magnetic field. Together with 3 walls, consisting of scintillator bars and measuring position and time of the passing particle, the time of flight (TOF) can be measured and the particle is identified from velocity and momentum [6].
To cover the angular gap between the central detector and the forward spectrometer several more detectors were built. The Scintillating Ring (SciRi), segmented into 96 plastic scintillator pads [7], and Daisy, an annular arrangement of multi-gap resistive plate chambers (MRPC), which is currently in preparation, cover the range from 8° to 25°.
At the very end of the experiment a photon flux measurement system complementing the tagging system measures the total photon flux at the target (see chapter 2.4), which is the topic of this thesis. The remainder of this chapter focusses on the photon tagging and flux measuring apparatus used for the photon flux determination.

[1] The coordinate system used in the experiment is shown in Fig. 2.2

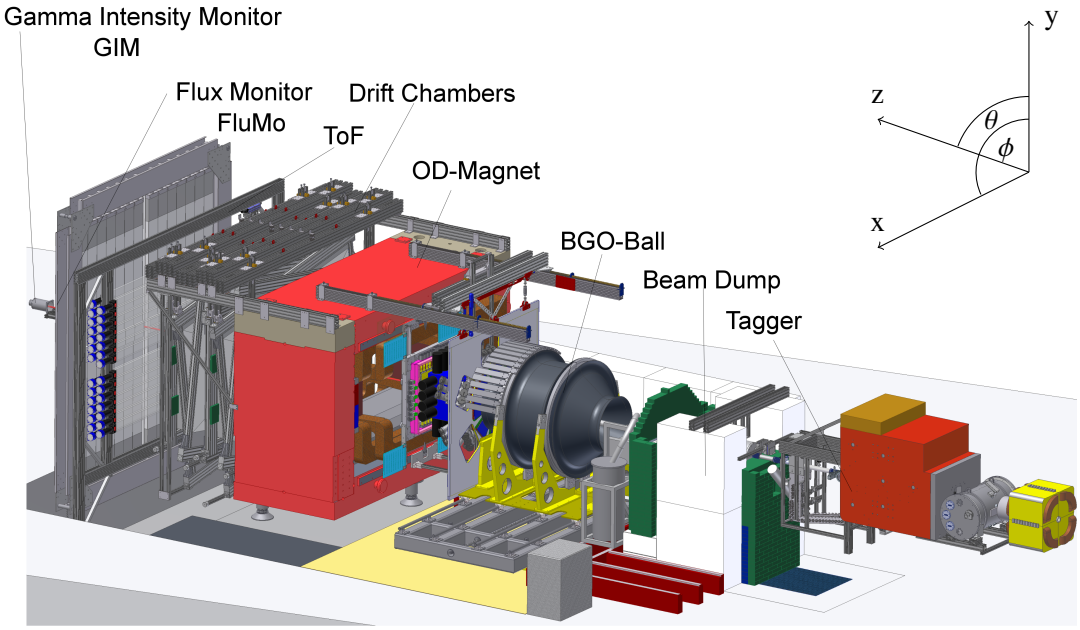

Figure 2.2: Overview of the BGO-OD experiment. The electron beam enters from the right and is converted to a photon beam which is incident upon a target in the center of the BGO-calorimeter. On the left side the forward spectrometer and the photon flux monitoring system are displayed.

2.3 Tagger

Very upstream of the experiment the incoming electron beam is converted to a real photon beam. This is done via bremsstrahlung, as the electrons are incident upon a radiator inside the goniometer. Different radiators can be placed in the beam, for example a copper radiator of 50 µm thickness ($0.0035X_0$) or a diamond radiator of 500 µm thickness, which corresponds to $0.004X_0$, for a linearly polarized photon beam. The lowest order bremsstrahlung diagrams are shown in Fig. 2.3.

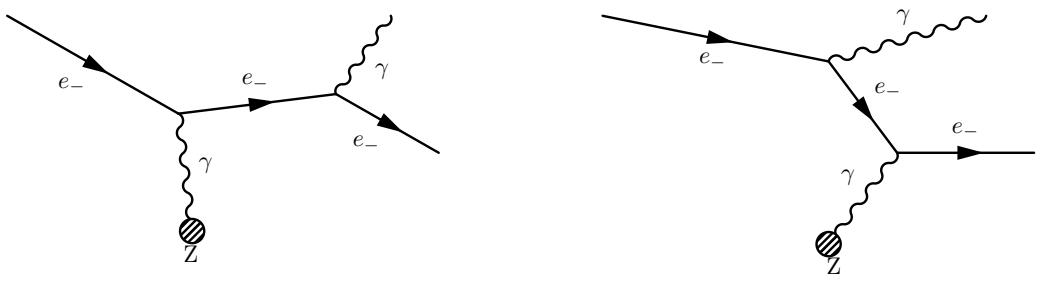

Figure 2.3: Feynman-diagrams of an electron producing a bremsstrahlung-photon on a nucleon.

An electron interacts with a nucleus and emits a photon. The energy needed for the photon reduces the kinetic energy of the electron:

$$E_\gamma = E_{beam} - E_{e^-}. \tag{2.2}$$

As the radiator is very thin, it can be assumed that every electron produces exactly one photon, which

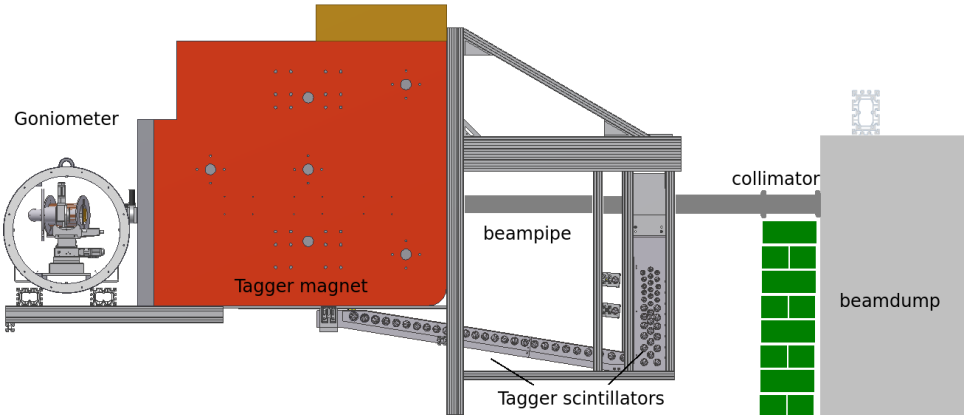

Figure 2.4: Overview of the tagging system. The beam enters from the left. The scintillators are shown in the lower right corner. Even further right the beam dump is visible.

allows the determination of the photon energy by measuring the electron energy. This is the task of the Tagger. It consists of the tagger magnet and 120 overlapping scintillator detectors. The electrons are subsequently detected by the array of scintillating detectors, and the electron energy is determined by the position of detection. The array covers the electron energies from 10% to 90% of the beam energy. The trajectory of the electrons curve in the magnetic field, the radius of which depends on the momentum of the electron. Due to space, the scintillators are divided in two sectors. 54 are placed in a horizontal construction, 66 more in the vertical plane (see figure 2.4). To reduce background a coincidence of two or three scintillators is required to count a hit. The 120 overlapping scintillators form 119 double coincidences and 118 triple coincidences, in total 237 possibilities to form coincidences. The Tagger scalers only consider double coincidences. Triple coincidences are sorted into both neighboring double coincidence channels. Tagger hits require a trigger and consider both, double and triple coincidences, but are limited by dead time.

The Tagger scintillators are read-out by two different types of photomultiplier-tubes (PMT). The channels for lower electron energies are equipped with ET Enterprise 9100SB PMTs. The channels for highest electron energies in the vertical plane are equipped with R7400U PMTs, which are more suitable for higher rates. This is necessary because the bremsstrahlung cross section is higher at higher electron energies (the cross section is to first approximation proportional to $\frac{1}{E_\gamma}$) and in addition the tracks of the electrons are getting closer together.[9]
Depending on their momentum the electrons are deflected on a different path and hit a different scintillator. After calibration [8], momentum and energy can be calculated from the hit position, which then allows the photon energy to be calculated from Eqn. (2.2). The electrons are stopped in the beam dump behind the scintillators. The photons that were produced at the radiator pass the magnet unaffected. These continue in a small cone ($\theta = \frac{m_e c}{E_{beam}}$[2]) around the former direction of the electron beam and pass through two collimators. A smaller collimator with a diameter of 3 mm is placed in front of the beam dump. The second collimator has a larger diameter of 12 mm and is placed right at the end of the beam dump. Due to this, the photon flux at the tagger is not the same as the flux at the target. This creates the necessity to measure the effective photon flux at the target that is available for reactions.

[2] θ is the characteristic angle of bremsstrahlung, m_e the electron mass, E_{beam} the electron beam energy

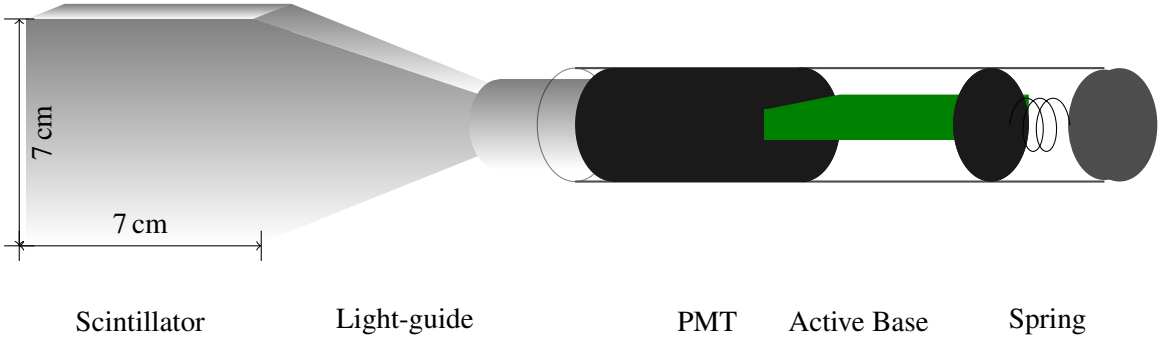

Figure 2.5: Design of a single FluMo. The scintillator on the left is placed in the beam.

2.4 GIM and FluMo

At the end of the experiment two detectors are used to measure the photon flux available to produce reactions in the target. They are called Gamma Intensity Monitor (GIM) and Flux Monitor (FluMo). The GIM is used for calibration at lower rates and the FluMo for a continuous measurement of the photon flux. While data is being taken only very few photons interact at the target and thus the flux at the end of the experiment can be assumed to be the same as it is at the target.

2.4.1 GIM

The GIM is a lead glass block using the Cerenkov effect to detect and fully absorb the electro-magnetic shower created by incident photons. Its dimensions are 6.5 cm x 6.5 cm x 30 cm. The length corresponds to 11 radiation lengths, and is such that it is 100% absorbing. The Cerenkov light is read out with a Hamamatsu 2083 PMT. The advantage of this detector is the possibility to measure the absolute photon flux directly. This works however only for small rates, i.e. small currents extracted from ELSA. At the highest expected rates of over 50 MHz in the tagger the detector saturates. Generally, it is possible to measure the photon flux at low rates and obtain the flux at high rates by scaling, as is it done at other experiments, e.g. at the Mainz Mikrotron[10]. There the beam size and divergence are very small and very stable. However this is prohibited by the ELSA extraction scheme. The ELSA beam parameters depend on energy and rate and the slightest change in the acceleration line can lead to large differences in the photon flux. Therefore an additional detector is needed, which is calibrated with the GIM and can be used at all photon rates. This is also a further benefit as the GIM suffers from radiation damage and can be removed from the beam when it is not explicitly needed. If it remained in the beam the high energetic radiation would destroy the lattice structure and decrease the transparency which of course leads to lower efficiency. Though the damage can be repaired by placing the GIM in the sunlight it is advantageous to avoid damage in the first place.

2.4.2 FluMo

The general idea of the Flux Monitor is to measure only a fraction of the absolute photon flux, which allows the detector to remain in the beam even at high photon rates and thus provide in-situ measurement of the flux. Intentionally, it is not total absorbing. It is made of Saint Gobain BC 404 plastic scintillators with a thickness of 0.5 cm and an area of 7 cm $\times$ 7 cm. The light is read out with ET Enterprise 9111B PMTs. The setup of a single FluMo is shown in Fig. 2.5. To one side of the scintillator a fish tail light guide is glued, transforming the rectangular shape of the scintillator to a circle, allowing the attachment

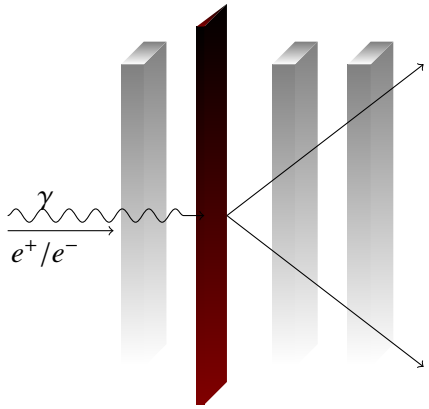

Figure 2.6: Schematic view of the original setup with three scintillators and a converter

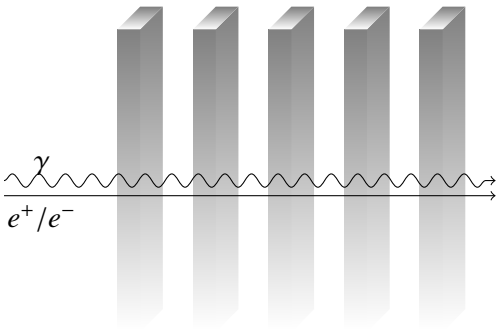

Figure 2.7: Schematic view of the improved setup with five scintillators

of a standard round PMT. A silicon patch ensures light contact between the light guide and the PMT. The PMT is operated with an active base, which provides stable operation at high rates. To ensure light tightness the light guide and scintillator are covered in aluminum foil and black tape. The PMT and its base are placed in an aluminum pipe. A cap at the end allows access to the electronics without dismantling the detector. For further details on the construction of the FluMo see [11].

In the original version the Flux Monitor consisted of three of these scintillators and a radiator, as shown in Fig. 2.6. The intention was to convert a certain fraction of the photons to electron positron pairs at the radiator and ignore everything that converted before. The first scintillator was used as a veto against already converted photons. To get a FluMo hit there had to be no veto signal, and the following two scintillators had to give a coincident signal. For this method to give stable results, one needs a veto efficiency of 100% or at least know the exact efficiency and correct for the inefficiency. The efficiency of each single scintillator changes however with rate and depends on the used thresholds. It can be much less than 100%. As a coincidence of the other two scintillators is required, a change in the detection efficiency of a scintillator affects the stability of the flux measurement. This of course leads to unknown errors and uncertainties on the measured photon flux. In the course of this work an improved method of measurement was developed and a modified detector setup was built.

The improved method does not use a converter, but explicitly uses the photons that converted to electron positron pairs somewhere upstream in the detector, that were vetoed before. It is unimportant how large the fraction of converted photons is, it is only important that it is stable and it is known. A FluMo hit is no longer defined by no veto and a double coincidence. Instead at least two out of three scintillators need to be coincident, where it is irrelevant which two. This way the flux measurement is less dependent on the detection efficiency of each single scintillator. To further improve the stability of the flux measurement two more scintillators are built to increase the sample. Then at least two or three out of five can be required to define a FluMo hit. This way the flux measurement becomes virtually independent of the detection efficiencies of the single scintillators.

CHAPTER 3

Photon Efficiency

It is essential for a correct photon flux to have a stable, reliable photon efficiency. The photon efficiency used here has to be distinguished from the detection efficiency of the scintillators. While the detection efficiency describes the probability to detect an electron-positron pair passing the detector material, the photon efficiency is the probability that a photon converts to an electron-positron pair somewhere upstream in the experiment which is then detected by the FluMo. The detection efficiencies of the single FluMos can however affect this. In the following chapter the photon efficiency is determined and its dependence on different parameters is discussed.

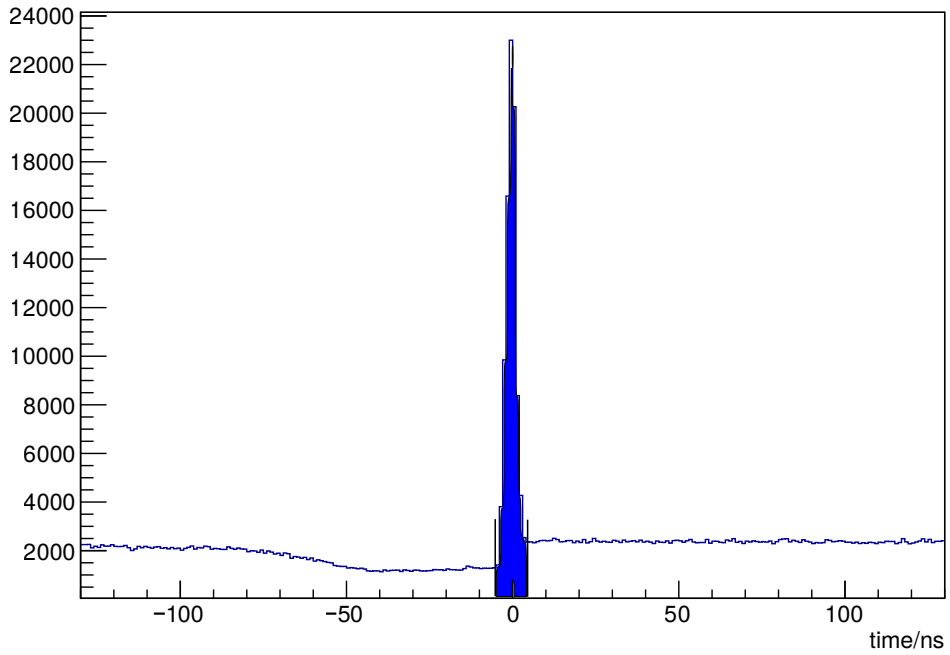

Figure 3.1: TDC spectrum with the meantime of all coincidences where at least 2 out of 3 FluMos were required. Shaded blue is the prompt peak that is used to determine the photon efficiency. The dip on the left side of the peak occurs due to dead time of the detectors.

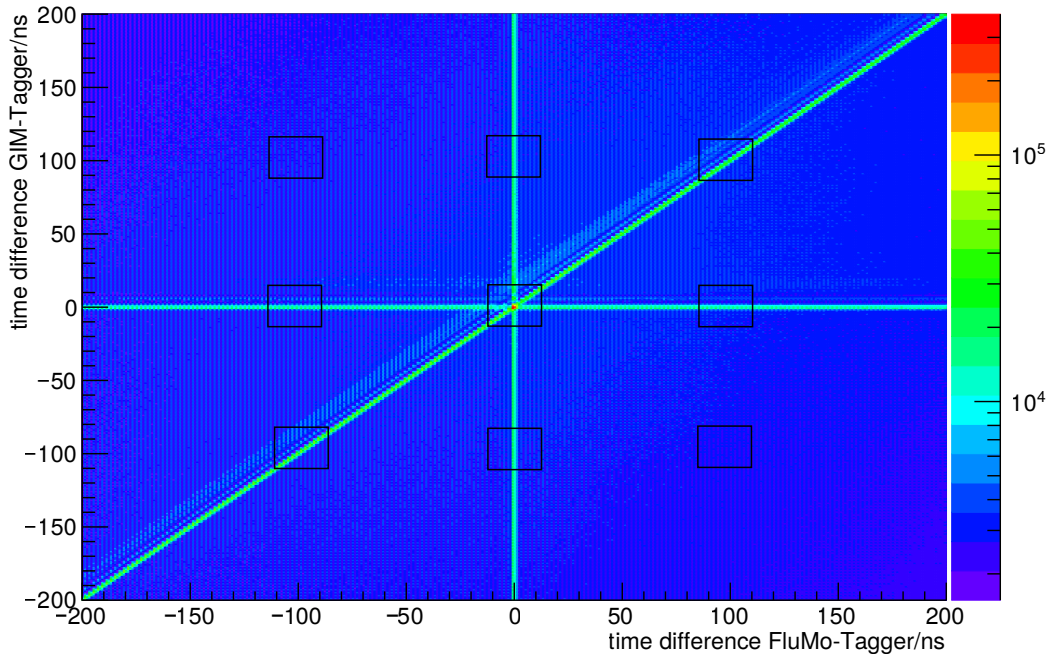

Figure 3.2: The plot depicts the time difference of two detectors respectively. On the x-axis the time difference of FluMo and Tagger, on the y-axis the time difference of GIM and Tagger is shown. The visible lines correspond to true coincidences of two detectors, at the intersection all three detectors coincide. The background consists of uncorrelated coincidences. The boxes indicate the boxes for the background subtraction.

If not stated otherwise all following plots are from run 28786. This run is one of several FluMo calibration runs taken during the data taking period in October and November 2015.[1] For these calibration runs the GIM is placed in the photon beam. In this data taking period only the original three scintillators were installed, but already analysed with the updated method. These data were chosen for this analysis, as they provide a lot of statistics, taken over a period of four weeks. Data with the updated FluMo setup has also been analysed, however there was only limited time for data taking, resulting in lower statistics.

The first step in determining the photon efficiency is to define a FluMo hit. The idea is to require only a subset of scintillators to give a coincident signal, though for comparison also the full set is taken into account. In Fig. 3.1 an example for a resulting spectrum, when requiring at least two FluMos, is shown. A FluMo hit is found by comparing the times in the TDC spectra of all FluMos. If there is a coincidence in a time window of ±3 ns the mean time is stored. This is done for at least two, at least three, at least four and all five FluMos. The centre peak around 0 ns contains the triggered events. These are the events used in further analysis. To obtain the photon efficiency one needs to compare the number of photons the FluMo counts to the number the GIM counts. Since the GIM is a total absorbing detector the fraction of these numbers is exactly the desired photon efficiency. As the photon efficiency might depend on energy it is advantageous to take the Tagger into account. By determining the photon efficiency for every Tagger channel independently, the energy dependence can be observed. This is done by finding all coincidences

[1] A data taking period consists of different type of runs for data taking and calibration. A FluMo calibration run usually contains 2.5 million events.

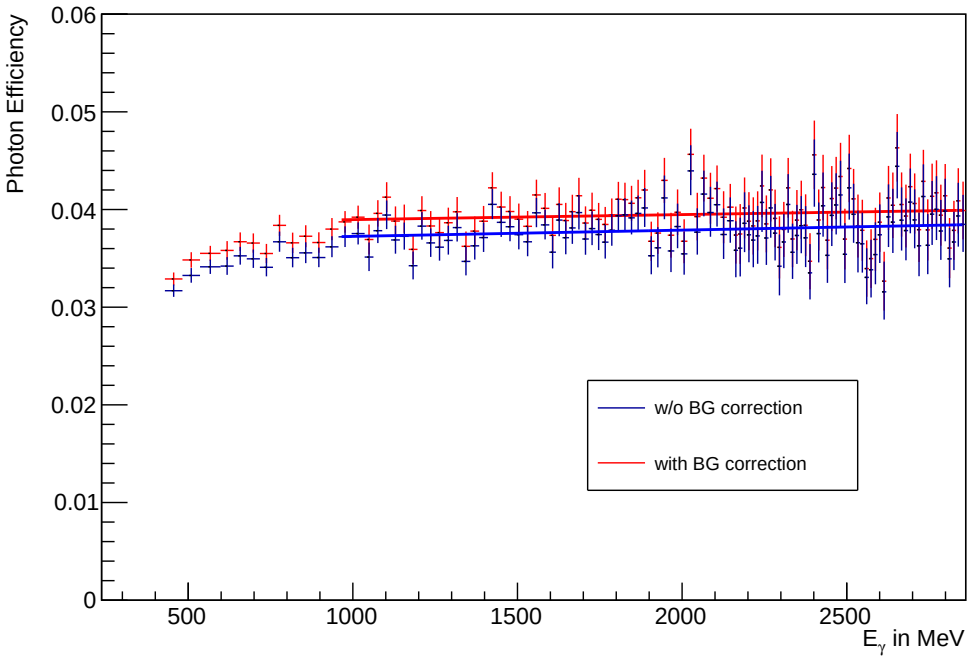

Figure 3.3: Photon efficiency as a function of energy. A background correction has been applied to the blue data. The comparison to the uncorrected photon efficiency (red data) shows a systematic increase.

of Tagger, GIM and FluMo and dividing them by the number of coincidences of Tagger and GIM. If Tagger and GIM both give a coincident signal the photon must have passed the FluMo. By counting the coincidences of Tagger, FluMo and GIM and dividing it by the coincidences of Tagger and GIM, the energy dependent photon efficiency is determined as depicted in Fig. 3.4.

$$\text{Photon efficiency} = \frac{\text{Tagger} \;\&\; \text{GIM} \;\&\; \text{FluMo}}{\text{Tagger} \;\&\; \text{GIM}}$$

Figure 3.4: The photon efficiency is determined from Tagger-GIM-FluMo coincidences divided by Tagger-GIM coincidences.

To reduce the background from uncorrelated coincidences one can look at all possible coincidences of Tagger, GIM and FluMo as shown in Fig. 3.2. On the x-axis the time difference of FluMo and Tagger is displayed, on the y-axis the time difference of GIM and Tagger. The histogram shows three lines, corresponding to the true coincidences of two detectors respectively. The coincidence of all three detectors is the intersection of all three lines. The number of coincidences at this point are the culmination of the true triple coincidences, the double coincidences (the lines) and the uncorrelated background. To subtract the double coincidences, boxes are drawn on the lines next to the central peak. One box is placed on each side of the peak to compensate for asymmetries. The content is then subtracted from this peak.

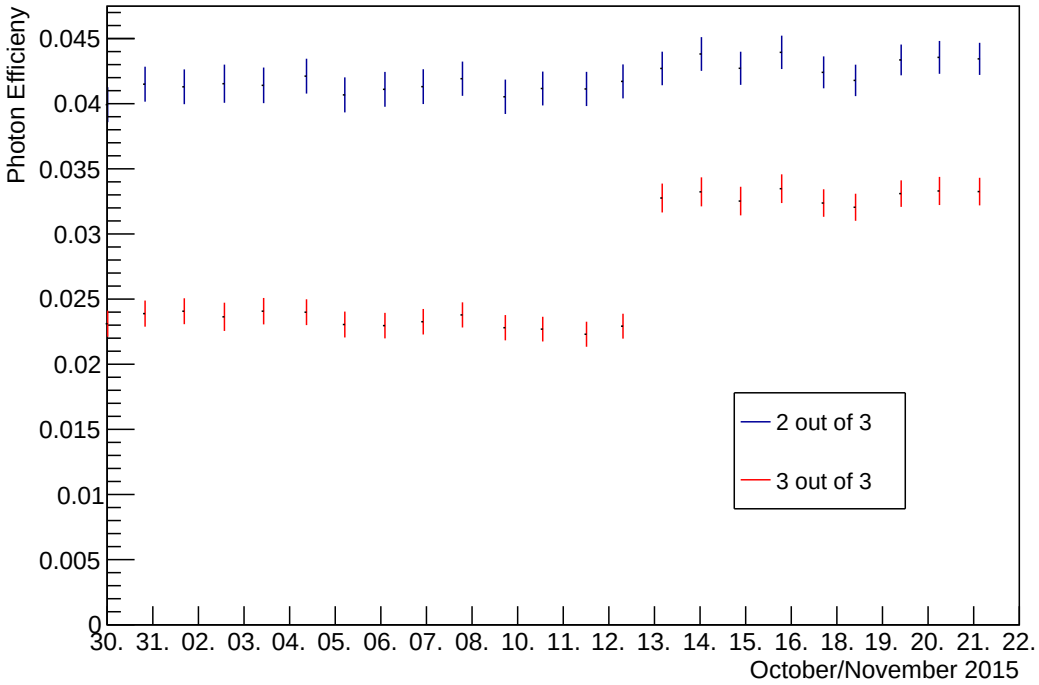

Figure 3.5: In the plot the maximum value of the photon efficiency, determined from a linear fit is shown for several data sets over the full data taking period in November 2015. For the blue data at least two out of three scintillators were required, for the red data all three.

As the boxes around the lines also contain uncorrelated background, this would be overcompensated. By drawing boxes around only uncorrelated background and adding the content again this can be corrected. The background correction of the Tagger-GIM coincidences is done in a similar but simpler way. Here the background can be assumed to be flat under the peak and can be averaged in a side band and the value subtracted from the peak. The photon efficiency before and after the correction is shown in Fig. 3.3. The corrected photon efficiency is systematically larger than the uncorrected, as one would expect. However the difference to the uncorrected photon efficiency is minimal. To get a comparable value a linear fit is applied to the channels 16 to 119. Due to saturation the first four Tagger channels are deactivated in this run, resulting in empty bins. For the fit the first 15 channels are excluded, as the photon efficiency is only linear after this point. From the fit the value at the highest measured energy (here 2 900 MeV) is obtained, assuming that this is the most stable point, as the rate is the lowest. These values are for the uncorrected photon efficiency 0.0384 ± 0.0013 and for the background corrected photon efficiency 0.0399 ± 0.0013. Within the statistical errors they are the same, though the systematic change remains.

To investigate the stability of the photon efficiency it is determined for several runs over the entire data taking period in October and November 2015. The result is shown in figure 3.5. The plot shows two different data sets. For the blue data at least two scintillators of a set of three were required. Within the statistical errors the photon efficiency is stable. For the second data set all three scintillators were required. The efficiency here is significantly smaller. This is expected, as the efficiency of each single scintillator is less than 100% and demanding a third decreases the chances of a coincidence. The photon efficiency however is not only smaller but shows a jump between the 12^{th} and 13^{th} November. Between

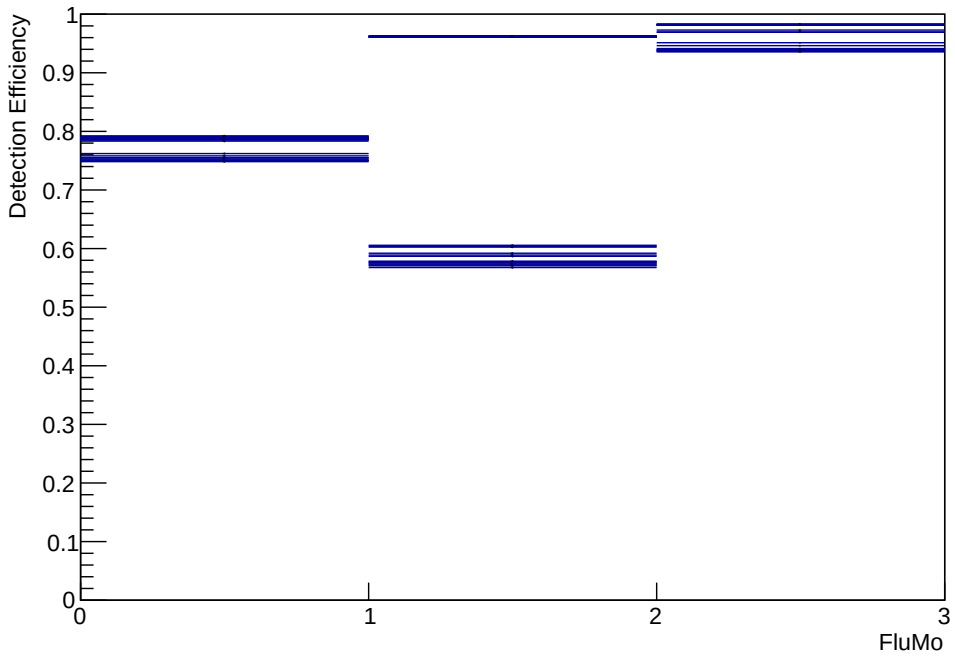

Figure 3.6: The plot shows the efficiencies of the original three scintillators for all runs of the data taking period in November 2015. The instability is clearly visible. Especially the second scintillator changed a lot after threshold setting.

these runs the thresholds of the scintillators were set to new values, thus increasing the photon efficiency determined from all three scintillators afterwards. The effect of the thresholds can be further understood when taking a look at the detection efficiencies of the three single scintillators. Fig. 3.6 shows the detection efficiencies of the three scintillators for every run shown already in Fig. 3.5. All three of them are not stable, but the second scintillator shows the largest difference. Here the setting of the threshold increased the detection efficiency massively. When requiring only two scintillators this difference does not affect the photon efficiency. This shows that the concept of requiring only a subset works already with only three scintillators and gives very stable results for the photon efficiency. The systematic error of the remaining instability is estimated to 0.2%. However, it can be further improved by adding more scintillators and being even less dependent on the single detection efficiencies.

In figure 3.7 the same analysis as before was repeated for data sets with five scintillators. It is not plotted as a function of time, but in dependence of the rate seen by the vertical part of the Tagger. Since the rate in the horizontal part is magnitudes smaller it can be neglected. It can be seen, that with increasing number of required scintillators the photon efficiency drops. When demanding at least two out of five it is mostly stable. When requiring at least three or at least four, all values are the same within the statistical error. The data for all five scintillators show the greatest instability as it was expected. Here every detection efficiency of the scintillators plays a role and affects the measured value of the photon efficiency. The reason for the small instability at 12.5 MHz is not clear. Since the photon efficiency determined from this run is lower for all numbers of scintillators there might have been an instability in the beam that went unnoticed. Problems in the ELSA vacuum system could have led to a varying beam quality when taking the data. Generally the improved method of determining the photon efficiency shows

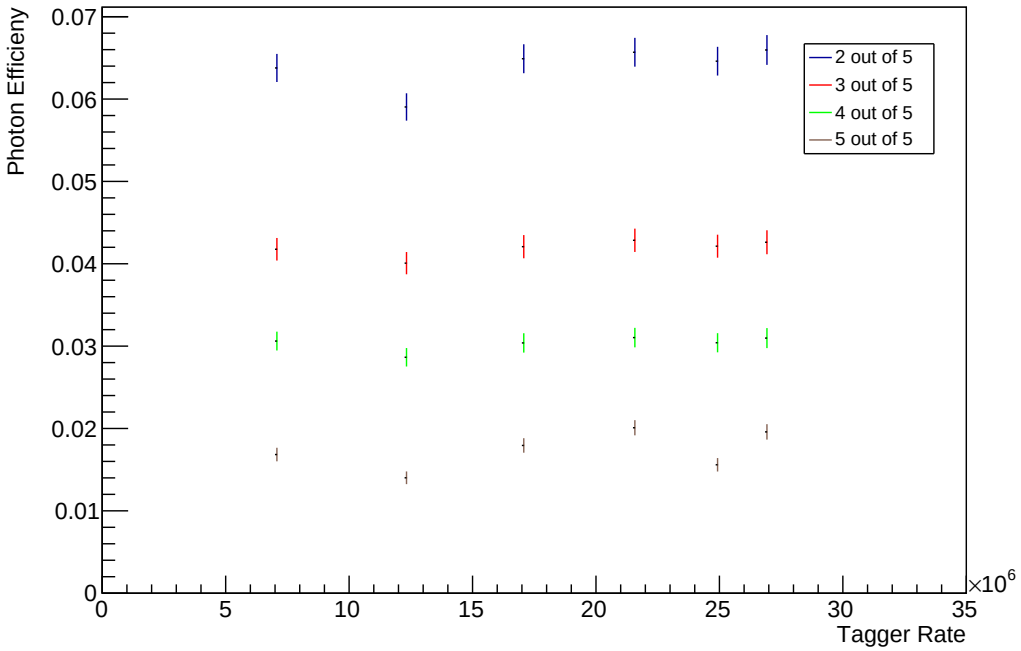

Figure 3.7: In the plot the maximum value of the photon efficiency, determined from a linear fit is shown for several data sets with the updated FluMo setup with five scintillators. The efficiency is plotted as a function of the Tagger rate for all numbers of required coincidences.

good results. The photon efficiency does not show a rate or threshold dependence any more. This now allows one to determine the tagging efficiency.

CHAPTER 4

Determination of the tagging efficiency P_γ

The tagging efficiency P_γ describes the probability that a tagged electron corresponds to a photon that is available for reactions at the target. The photon flux at the target is reduced, compared to the photon flux at the Tagger, due to collimation. In this chapter the tagging efficiency will be determined from experimental data and simulation. Furthermore, the importance of a good alignment of collimator and photon beam will be discussed.

4.1 P_γ from experimental data

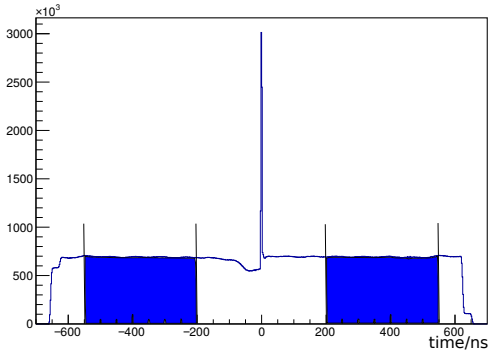

Figure 4.1: TDC time spectrum of the Tagger. The central peak contains triggered events. To avoid artifacts from trigger requirements not this peak, but the sidebands shaded in blue are used for determining the tagging efficiency.

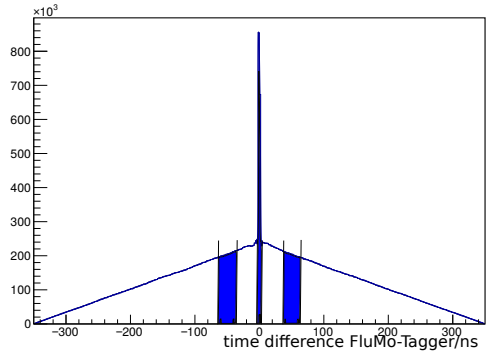

Figure 4.2: Time difference of Tagger and FluMo. The central peak contains true coincidences and background of uncorrelated coincidences. This background is determined with boxes (shaded in blue) and subtracted.

Generally, the tagging efficiency is determined by dividing the photon flux available at the target by the electron flux at the Tagger. The photon flux at the Tagger is equivalent to the number of tagged electrons[1]. The photon flux at the target has to be determined from the number of photons detected by the FluMo and the photon efficiency, which was already determined in chapter 3. While for the photon efficiency special calibration runs were needed, the tagging efficiency can be determined from any run

[1] Only true within the tagged energy range of 10% to 90% of the beam energy. Only this energy range is analysed

$$\text{Tagging efficiency} = \frac{\boxed{\text{Tagger}} \;\&\; \boxed{\text{FluMo}}}{\boxed{\text{Tagger}} \times \boxed{\text{photon efficiency}}}$$

Figure 4.3: The tagging efficiency is determined from Tagger-FluMo coincidences divided by Tagger hits and photon efficiency.

where FluMo and Tagger were read out. To avoid artifacts caused by special trigger requirements, not the prompt peak, but the side bands are used for determination of the tagging efficiency. Fig. 4.1 displays the entire TDC spectrum of the Tagger. Shaded in blue are the parts of the side bands that are used for further analysis. The limits are chosen such, that only flat parts are used and for example, regions with dead time effects are excluded. For the photon flux at the target, the same side bands are selected from the FluMo TDC spectrum. To be able to observe an energy dependence Tagger-FluMo coincidences are required. The time difference of Tagger and FluMo is shown in Fig. 4.2. The central peak contains the true coincidences over a background of uncorrelated coincidences. The triangular shape is caused by the limits of the sidebands of 350 ns. A time difference of more than 350 ns is not possible. The smaller the time difference, the larger the chance to find a pair. This triangular background is subtracted by placing boxes left and right of the peak. This way the background is not described perfectly, though by placing the boxes very close to the prompt peak the difference is minimized. In a distance of ±50 ns two boxes of ±15 ns are placed. The prompt peak is cut at ±1.5 ns. The boxes for background subtraction are chosen larger than the the cut on the prompt peak to gain more statistic and average over several bunches. The width of the bunch structure of the accelerator is of the size as the cut on the prompt peak. A box size of ±1.5 ns would select only a single bunch and might lead to errors on the background correction. This method still underestimates the background, which leads to an estimated systematic error of 2%. The corrected number of Tagger-FluMo coincidences at the target is then divided by the photon efficiency and the photon flux at the Tagger (see Fig. 4.3).
Fig. 4.4 shows the result determined from run 31917 of the October/November data taking period. This is a standard data taking run containing 500000 events at a beam energy of 3 200 MeV. Plotted in blue is the tagging efficiency determined when requiring at least two out of three FluMo scintillators, plotted in red is the tagging efficiency when requiring all three scintillators. Within the statistical errors the tagging efficiency determined from at least two and all three are the same, as it is expected if the determination is correct. The tagging efficiency shows no energy dependence. The Tagger channels for the smallest photon energies can show saturation effects, as it was already the case at the photon efficiency, though this should cancel out in the analysis. The stability of the tagging efficiency is observed by fitting a constant to channels 16 to 119 for a selection of runs over the entire data taking period. The result is shown in Fig. 4.5. The error shown here is not the error of the fit, but the one sigma width of the distribution around the fit value. Within these errors the tagging efficiency is quite stable. However there are two higher values towards the end of the data taking period. It can not be an effect of the photon efficiency, as this was proven to be stable in chapter 3. There is also no difference between requiring at least two or three FluMo scintillators. The exact reason is unclear, however the most likely reason is a shift of the electron beam. This was rather unstable during these two days. How this could affect the tagging efficiency will be discussed in chapter 4.3.
As within the error bars, the tagging efficiency determined from at least two scintillators is the same as

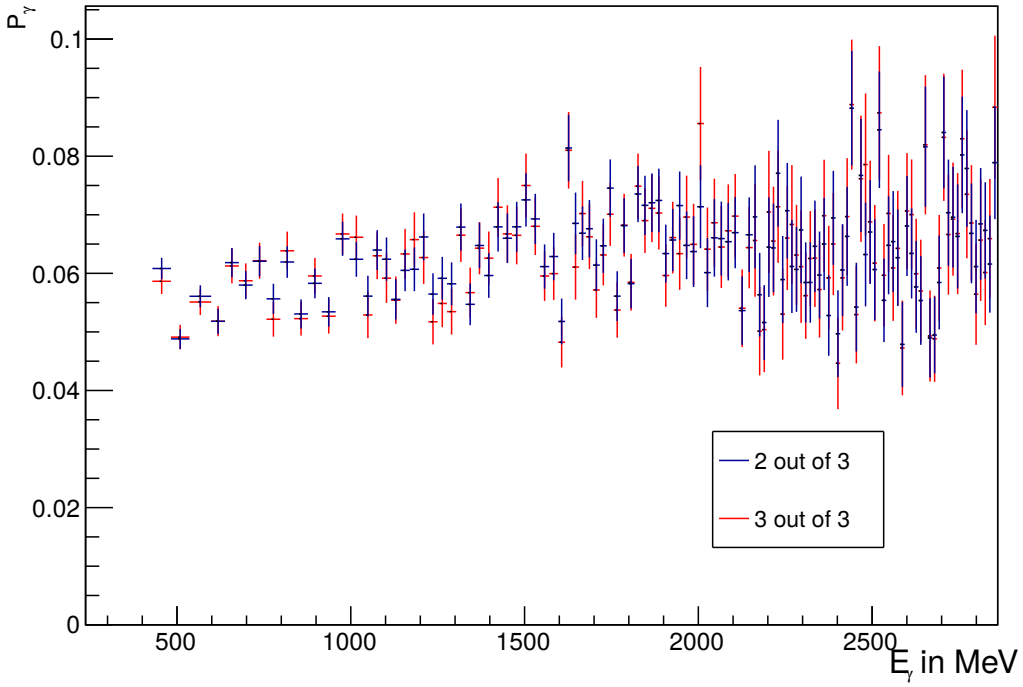

Figure 4.4: Tagging efficiency determined from run 31917 as a function of photon energy. Shown in blue is the tagging efficiency determined from at least two scintillators, in red the tagging efficiency requiring all three.

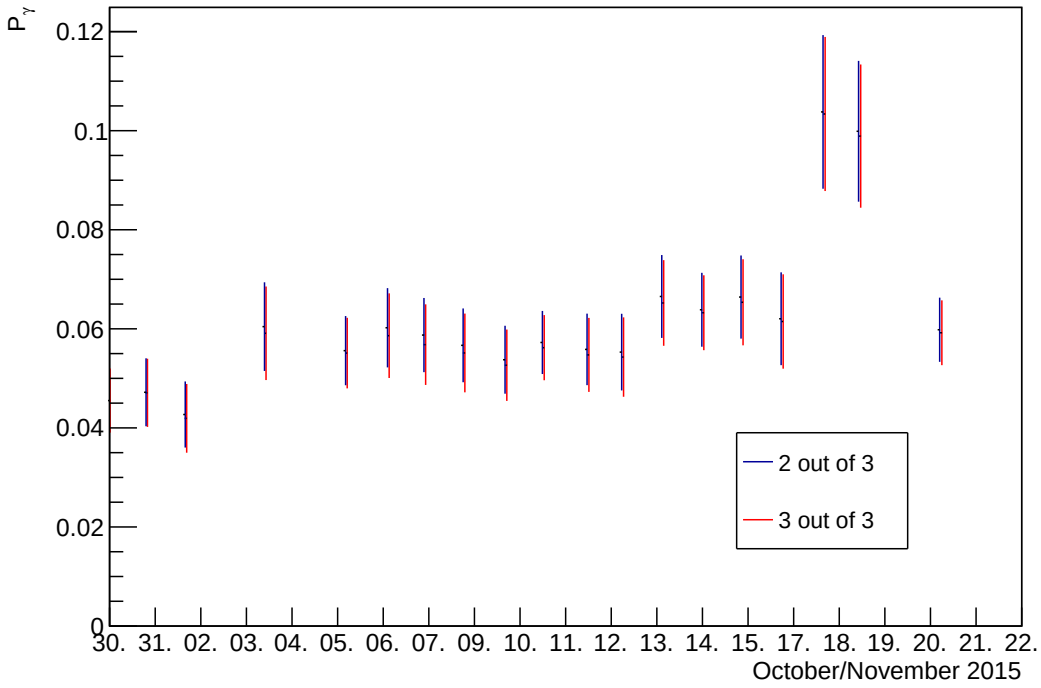

Figure 4.5: Tagging efficiency for a selection of runs over the entire data taking period. Shown in blue is the tagging efficiency determined from at least two scintillators, in red the tagging efficiency requiring all three. The blue data is shifted to the left so both data sets are visible.

the one with all three scintillators, this would in principle allow to use both. The advantage of requiring only two is the possibility to average over the entire data taking period instead of doing the analysis run by run, as it would be necessary with an unstable photon efficiency. The values for the tagging efficiency obtained in this chapter are lower than expected. Simulations suggest a significantly larger tagging efficiency. This is discussed in the next subsection. Also a misalignment of collimator and beam will be studied as a possible reason for the different results.

4.2 Simulation of P_γ

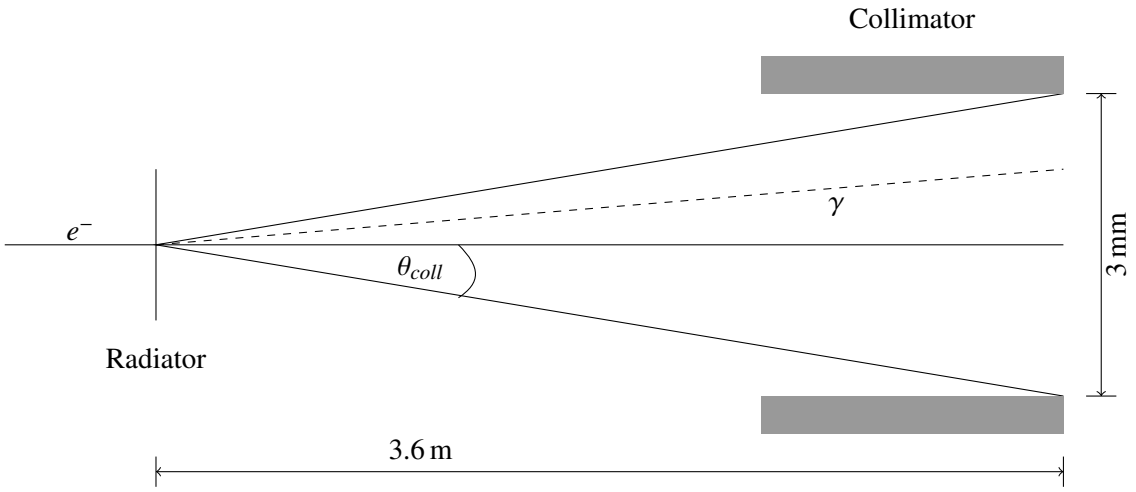

Figure 4.6: Collimation of the photon beam at the BGO-OD experiment. The electron beam coming from the left is converted to photons at the radiator. At a distance of 3.6 m a collimator is placed. The sketch is not to scale.

A simulation of the photon flux is important to understand the experimental data. Several parameters are important. The size of the beam spot at the radiator needs to be known, the divergence of the electrons and the characteristics of bremsstrahlung. Beam spot size and divergence can be directly inserted into the simulation as fix parameters.
The beam spot can be measured at the radiator and has a one σ width of 1.3 mm in x and 0.35 mm in y. The beam divergence contains the divergence of the electron beam before the radiator and the divergence caused by the radiator due to multiple scattering. It depends on the length of the used radiator and the beam energy. At a beam energy of 3 200 MeV the divergence of the electron beam was estimated to 0.3 mrad in x and 0.08 mrad in y [12]. The divergence caused by the radiator can be calculated from $\theta_0 = \frac{13.6\,\mathrm{MeV}}{\beta c p} z \sqrt{\frac{x}{X_0}} \left(1 + 0.038 \ln \frac{x}{X_0}\right)$. Here βc, p and z are the velocity, momentum and charge number of the incident particle. $\frac{x}{X_0}$ is the thickness of the radiator in radiation length[13]. With a diamond or copper radiator with a length of $0.004 X_0$ the total beam divergence at 3 200 MeV has a value of 0.37 mrad in x and 0.22 mrad in y.
The characteristics of bremsstrahlung are a little more complicated. The energy and angular dependent

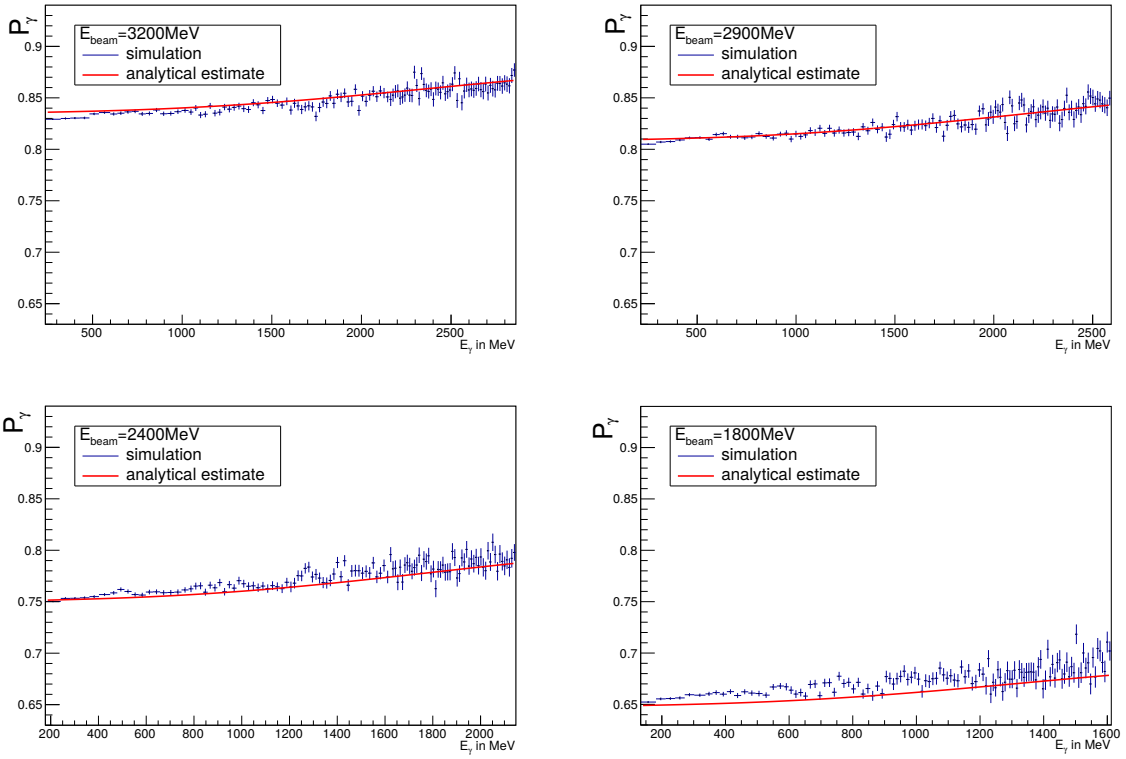

Figure 4.7: Simulated and analytically determined tagging efficiency for different beam energies. The analysis is done for an ideal beam where beam spot and beam divergence are zero.

bremsstrahlung cross section for a given beam energy is given as:

$$\sigma_{LL}(k,x) = 8Z^2\alpha r_e^2 \frac{dk}{k}\frac{E}{E_0}\frac{xdx}{(1+x^2)^2}\cdot \left(\left[\frac{E_0}{E}+\frac{E}{E_0}-\frac{4x^2}{(1+x^2)^2}\right]\log\frac{2EE_0}{m_e k}-\frac{1}{2}\left[\frac{E_0}{E}+\frac{E}{E_0}-\frac{16x^2}{(1+x^2)^2}\right]\right) \tag{4.1}$$

with E_0 and E being initial and final energy of the electron, k the final energy of the photon, $x = \frac{E_0\theta}{m_e}$ [14]. To first approximation $E_0 = E + k$. Thus the final electron energy can be eliminated and the function only depends on the final photon energy and the angle θ, as E_0 is determined by the beam energy. The distribution in ϕ is uniform.
The simulation includes a modelling of the detector parts of the BGO-OD experiment using Geant4. The photon beam is created at the radiator with the given beam spot size and by choosing random pairs of photon energy and theta following the distribution of Eqn. (4.1) for every single photon. To the angles θ and ϕ from bremsstrahlung, the angles θ_{e^-} and ϕ_{e^-} describing the divergence of the electron beam are added respectively. The simulation also allows to move the collimator and rotate it to simulate a misalignment.

The tagging efficiency P_γ can be calculated analytically as the fraction of the number of the photons in a cone passing through the collimator divided by the number of all photons. The angle θ_{coll} in which the photons can pass the collimator is determined from the distance to the collimator and its radius (as defined

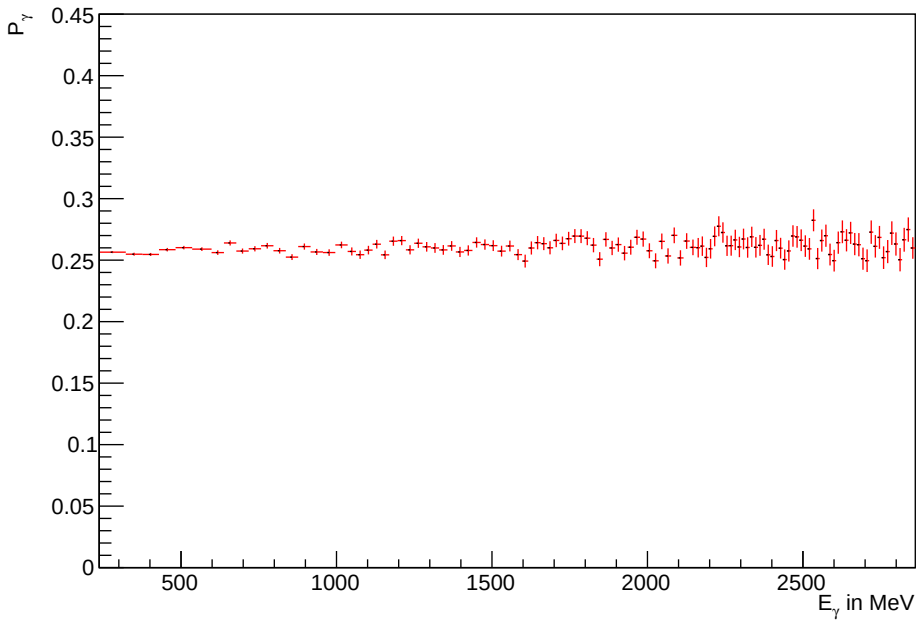

Figure 4.8: Simulated tagging efficiency for a beam energy of 3 200 MeV. Here a realistic beam size and beam divergence are included in the simulation.

in figure 4.6). The collimator is placed in a distance of 3.6 m and has a diameter of 3 mm. Normalized to the characteristic angle of bremsstrahlung $\theta_c = \frac{m_e}{E_0}$ the photon beam is limited within the fraction

$$\bar{x} = \frac{\theta_{coll}}{\theta_c} = 0.27 \tag{4.2}$$

for the maximum beam energy of 3.2 GeV. To analytically obtain the tagging efficiency the bremsstrahlung cross section as stated in Eqn. (4.1) is integrated over the angle x from 0 to $\bar{x}$ and divided by the integral over the solid angle:

$$P_\gamma = \frac{dk \int_0^{\bar{x}} \sigma_{LL}(k,x)dx}{dk \int_0^{\infty} \sigma_{LL}(k,x)dx}. \tag{4.3}$$

In this calculation the beam spot size is zero as is the electron beam divergence. This has to be considered when comparing the results to simulation. In Fig. 4.7 the simulated and analytically determined tagging efficiency is shown for four different beam energies. The red line shows the analytical estimate, the blue data contain 10 million simulated events each. Generally, the line fits to the simulated data. For the lowest energy the simulated tagging efficiency is slightly too high, though in the other cases shape and value of the analytical calculation are within the statistical errors of the simulation. At least in the case of an ideal beam and not too low beam energy, the simulation describes the tagging efficiency well.
For the real beam the beam divergence and beam spot size can not be ignored. Including these parameters decreases the tagging efficiency significantly. Fig. 4.8 shows the simulated tagging efficiency for a beam energy of 3 200 MeV, a beam spot size of 1.3 mm in x and 0.35 mm in y and a beam divergence of 0.37 mrad in x and 0.22 mrad in y. Not only the absolute value has changed. The shape of the tagging efficiency is quite flat now and shows no energy dependence any more. This shape is similar as the shape

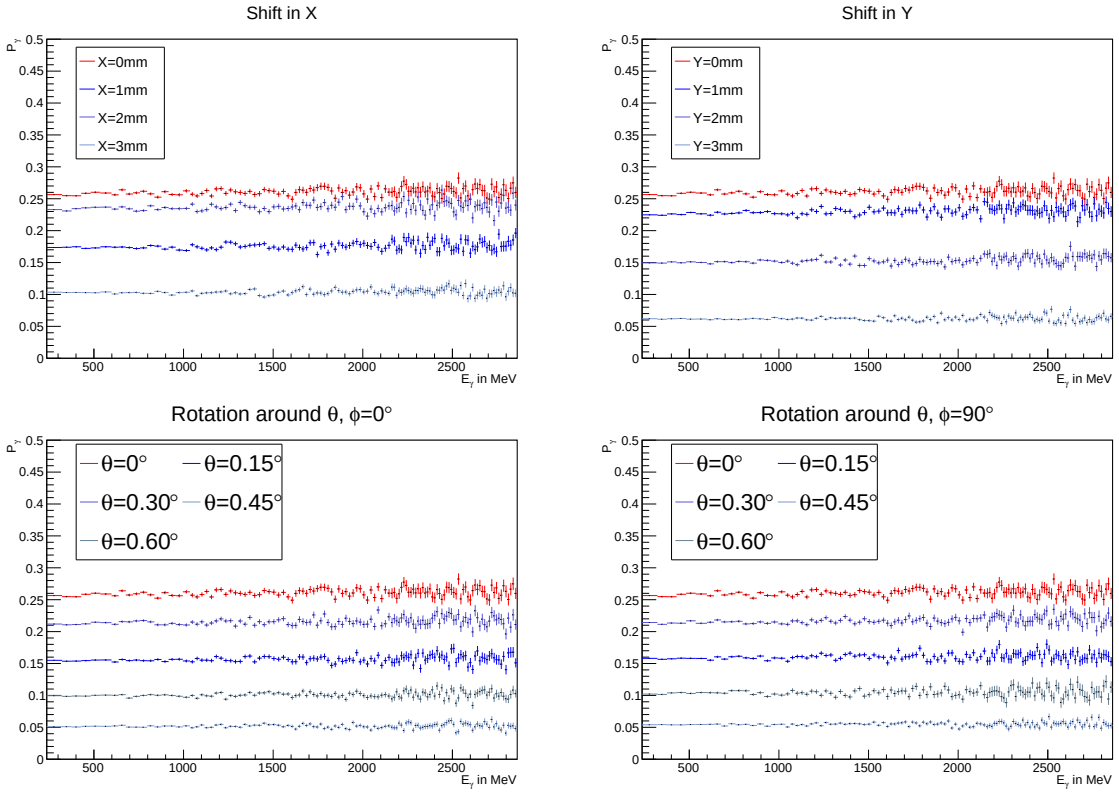

Figure 4.9: Simulation of the tagging efficiency for different collimator positions. The collimator is either shifted in x or y, or rotated around θ.

of the experimental data. The absolute value of the tagging efficiency from experimental data however is much smaller than the simulation. Reasons for the difference might be a wrong beam spot size, a wrong electron beam divergence or a bad alignment of beam and collimator. The most likely reason for the large difference between simulation and experimental data is a misalignment of collimator and beam. A simulation of a shift or rotation of the collimator supports this hypothesis.
Fig. 4.9 shows the tagging efficiency for different shifts in x and y. In both cases the tagging efficiency can be significantly decreased by a small change in the position. However, the decrease shows a dependence on the direction of the shift. Since the beam is broader in x than it is in y, a shift in this direction shows less effect than in y-direction. A shift of 3 mm in x is not enough to explain the decrease in the tagging efficiency, whereas a shift of 3 mm in y might explain the difference sufficiently. The collimator could not only be shifted, but also rotated. In Fig. 4.9 the tagging efficiency is also simulated for several rotation angles around θ. A rotation around θ of roughly 0.6° is enough to decrease the tagging efficiency to under 10%. Obviously the collimator could not only be misaligned in one direction. A mixture of shift and rotation in all direction can result in the same decrease in tagging efficiency. This demonstrates, that a tagging efficiency of the order of the measured one can be easily explained by collimator misalignments. The strength of the effect underlines the importance of an alignment of beam and collimator and in-situ monitoring during data taking. The position of collimator and beam shall be analysed and optimised in the next chapter.

4.3 Optimization of P_γ

In this chapter the importance of a good alignment of beam and collimator will be investigated and the positioning will be optimised. The data are taken at a beam energy of 1 800 MeV. The first step for a good alignment of collimator and beam will be to align the beam as well as possible with the beam pipe. A perfectly straight collimator is of no help if the beam passes it at an angle. This is done without collimator, to be able to see the entire beam. In a next step the collimator is inserted and moved until the best position is found. To observe the beam a silicon strip detector is placed in the beam right behind the second collimator. This second collimator has a diameter of 12 mm and will remain in place, its diameter is large enough to allow this. The first collimator is placed inside the beam pipe in front of the beam dump (see Fig. 2.4). This part of the beam pipe can be moved in the vertical plane with the help of two screws. In the horizontal plane two linear tables allow to adjust the front and rear part of the collimator separately.
In the first step this collimator is removed from its position to observe the full beam. Fig. 4.10 shows the beam spot on the silicon detector without collimator. The detector is not centred, thus the centre of the beam spot not being in the centre of the detector does not mean the beam is badly positioned. Since the holding structure of the collimator does not simply allow movements in vertical direction, it will only be moved in the horizontal plane. Fig. 4.11 depicts a projection of the beam spot on the x-axis. The jump in the shape at ±0.3 mm has nothing to do with the shape of the beam, but with the efficiency of the different parts of the detector which change at this position. The edges at −0.5 mm and 0.7 mm however are caused by the second collimator. The centre of the beam is located at 0.1 mm, thus the beam is practically centred with respect to the second collimator.
In a next step the first collimator is reinserted into the beam pipe. Whereas its diameter was 3 mm in earlier data taking, for the future, a larger diameter of 7 mm will be used to further increase the tagging efficiency. Fig. 4.12 shows the beam spot with the collimator inserted. Obviously it is very badly aligned. The centre of the beam is cut away by the 7 mm collimator, only a part a the edge of the beam can pass through it. Yet the projection in Fig. 4.13 is nearly Gaussian and could be mistaken for a good beam. This shows, that even if the beam looks good, the collimator might be badly misaligned.
The collimator is then aligned with the photon beam. When looking at Fig. 4.14 one sees, that the size of the beam spot is much larger and the centre is at the same position as the centre of the entire beam. To achieve this the collimator was not only shifted, but also rotated. In Fig. 4.15 the width of the beam spot is much larger than it was before. The shape is symmetric around the centre of the beam. In this position the beam pipe with the collimator inside is fixed to an aluminium plate, which is built into the beam dump, to avoid unwanted movement.

After aligning collimator and beam, the tagging efficiency is determined and compared to simulation again. Fig. 4.16 shows the simulated tagging efficiency without the first collimator (red) and the tagging efficiency determined from experimental data without the first collimator (blue). Fig. 4.17 shows the tagging efficiency with completely misaligned collimator. Fig. 4.18 depicts the tagging efficiency with well aligned collimator for simulation (red) and experimental data (blue). As expected the largest tagging efficiency is reached without collimator, the smallest tagging efficiency corresponds to a badly aligned collimator. Notable is the large discrepancy between simulation and experimental data with as well as without first collimator. Compared to simulation, the measured tagging efficiency still appears much too small. The reason for this is not entirely clear. One reason could be a beam divergence larger than assumed in the simulations. At a beam energy of 1 800 MeV the divergence is expected to 0.48 mrad in x and 0.39 mrad (see Chapter 4.2). In Fig. 4.16 and Fig. 4.18 the tagging efficiency is simulated with a factor three multiplied to the beam divergence. This could explain the difference between simulation and experimental data.

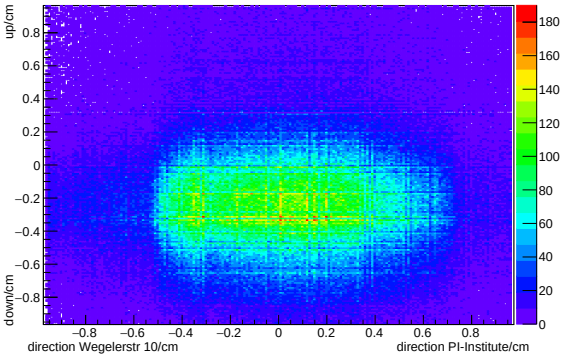

Figure 4.10: Beam spot without first collimator.

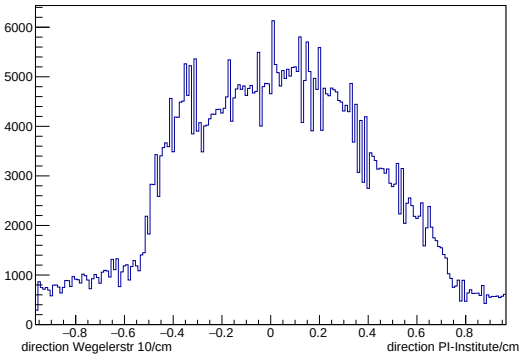

Figure 4.11: projection on the x-axis of the beam spot without first collimator.

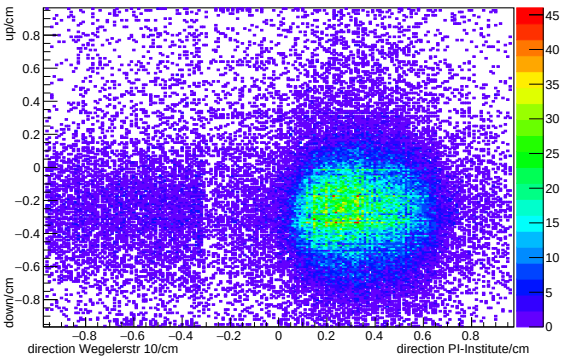

Figure 4.12: Beam spot with badly aligned first collimator.

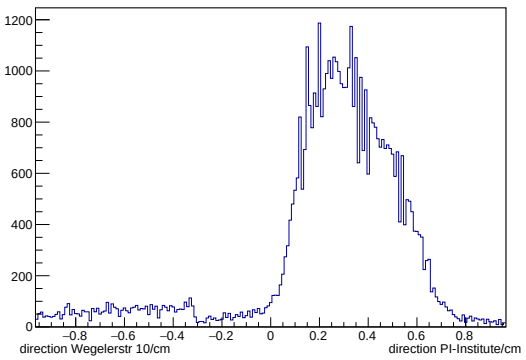

Figure 4.13: projection on the x-axis of the beam spot with badly aligned first collimator.

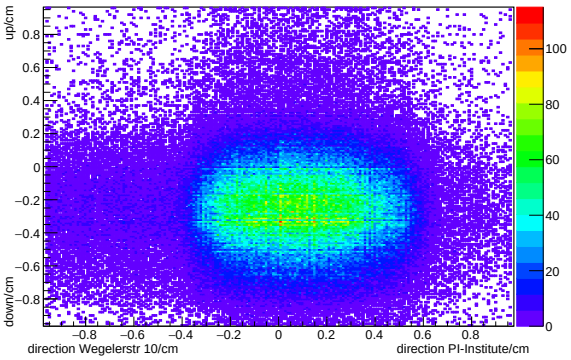

Figure 4.14: Beam spot with well aligned first collimator.

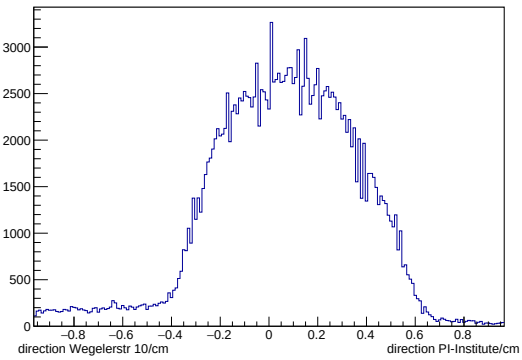

Figure 4.15: projection on the x-axis of the beam spot with well aligned first collimator.

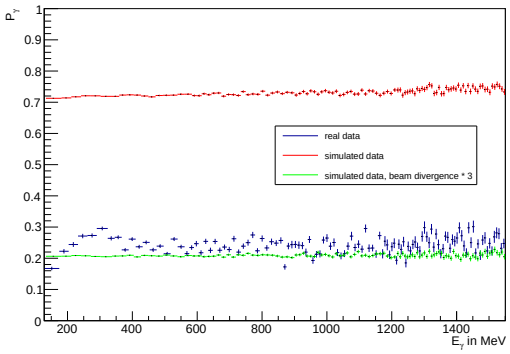

Figure 4.16: Tagging efficiency from experimental data (blue) and simulation (red) without collimator. For the simulated green data the beam divergence was multiplied with a factor three to fit the experimental data.

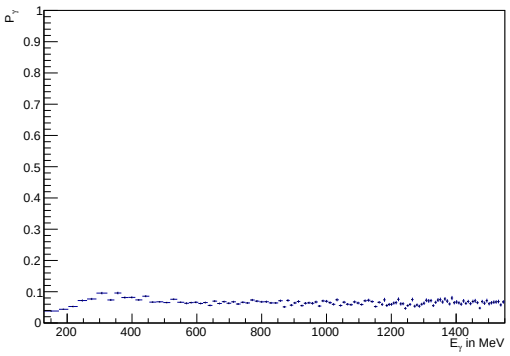

Figure 4.17: Tagging efficiency from experimental data with badly aligned collimator.

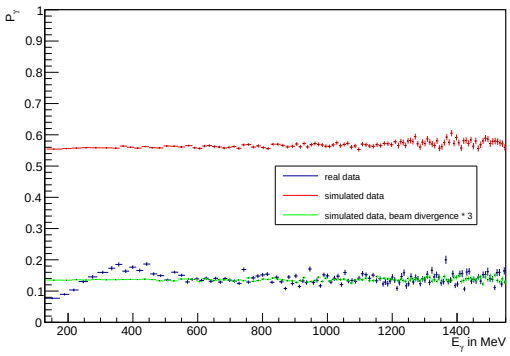

Figure 4.18: Tagging efficiency from experimental data (blue) and simulation (red) with well aligned collimator. For the simulated green data the beam divergence was multiplied with a factor three to fit the experimental data.

To check the plausibility of this divergence, the emittance can be determined and compared to the values measured at ELSA. The emittance describes the volume of the beam in phase space and can be calculated as the product of beam size and electron beam divergence before passing the radiator. From the original values used in simulation an emittance of 399 nm rad in x and 27.8 nm rad in y is determined. The values measured at ELSA are 400 nm rad in x and 36 nm rad in y for a beam energy of 1 600 MeV [15]. So the emittance from the parameters used here is of the right magnitude. Since the beam energy for the measurements at ELSA was a bit lower and emittance increases with energy, a larger beam divergence may be possible. A factor of three however appears very large. What could additionally decrease the tagging efficiency is the energy spread of the beam in the accelerator. The beam line is not achromatic, meaning deflection and focussing is energy dependent. Particles with energies off the design beam energy are not focussed on the design beam line, causing a dispersion of the beam. To fully understand the discrepancy between simulation and experimental data further analysis is necessary, larger values for the dispersion however appear plausible.

As a check that the tagging efficiency is correctly determined a well known cross section will be determined in the next chapter.

CHAPTER 5

$\gamma p \to \pi^0 p$ Cross Section

Since the results for simulated tagging efficiency and experimental data are very different, another cross check is necessary. In this chapter the well known cross section $\gamma p \to \pi^0 p$ will be extracted and compared to the results of the Bonn-Gatchina partial wave analysis. This reaction is chosen because it has a large cross section and a relative simple signature.
One has to differentiate between the total cross section covering the full angle and the differential cross section in a certain angular region. Here only the differential cross section for several bins in $\cos(\theta)$ shall

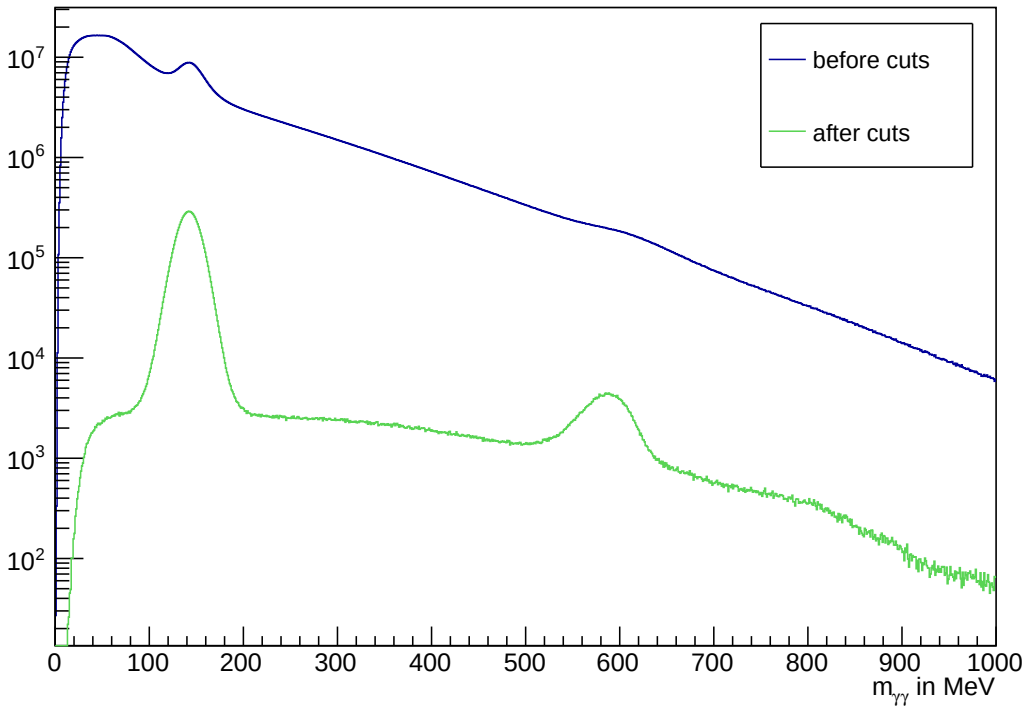

Figure 5.1: Number of photon pairs as a function of their invariant mass. In blue the full data set is shown, the green set shows the data after several selective cuts have been applied to reduce background.

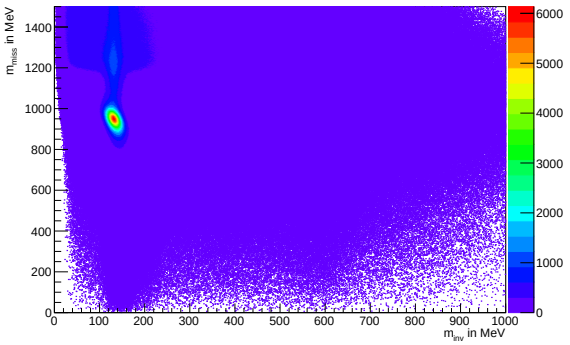

Figure 5.2: Spectrum of the missing mass versus two photon invariant mass. A peak is visible at the π^0 mass in the invariant mass spectrum and at the proton mass in the missing mass spectrum.

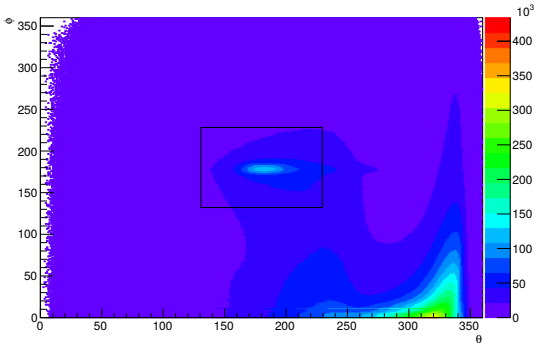

Figure 5.3: Angular distribution between π^0 and p-candidates in ϕ and θ. The box indicates the three σ width of the peak at 180° in θ and ϕ.

be determined. It is only used as a test, so that it is not necessary to integrate over all cos(θ)-bins to get the total cross section. Since the photon flux is energy dependent, the differential cross section is also determined energy dependent.

5.1 Cross Section Formula

The cross section is determined according to

$$\frac{d\sigma}{d\Omega} = \frac{\text{absolute number } \pi^0(E,\theta)}{\text{absolute photon flux}(E) \times \delta \times \Delta\Omega} = \frac{\text{detected number } \pi^0(E,\theta) \times \frac{1}{\text{detection efficiency}(E,\theta)}}{\text{Tagger scalers}(E) \times \frac{1}{\text{tagging efficiency}(E)} \times \delta \times \Delta\Omega} \tag{5.1}$$

with $\delta = 2.53 \times 10^{23} \frac{1}{\text{cm}^2}$ the target area density. In a first step, π^0 and p are reconstructed. Next, the detection efficiency is determined. Finally the photon flux is obtained before extracting the differential cross section.

5.1.1 $\pi^0 p$ reconstruction

In this analysis only the π^0 is required to be seen directly in the BGO-ball. The proton is reconstructed indirectly by identifying it in the missing mass spectrum. In over 98% of the cases, the π^0 decays to two photons[13]. These photons create electro-magnetic showers in the crystals of the BGO ball. The energy deposit is not restricted to a single crystal, but usually includes several. By forming them into clusters the full energy deposit and position of the incident particle can be determined. From the position in the BGO ball the direction of the photon is reconstructed. In their rest frame, both photons need to be at an angle of 180°. Apart from that, they need to be in a certain time window to form a pair. The invariant mass of the photon pair is then determined from $m^2_{\gamma\gamma} = (E_1 + E_2)^2 - (p_1 + p_2)^2$. By requiring no hit in the scintillator barrel, charged particles are excluded. Fig. 5.1 shows the number of reconstructed photon pairs as a function of their invariant mass (blue). The spectrum already shows a small peak at the π^0 mass of 134.98 MeV. However, most of the data is background, therefore certain cuts need to be applied to the data to select the true π^0.
The complete final state of the reaction contains two photons and a proton. This proton is not required

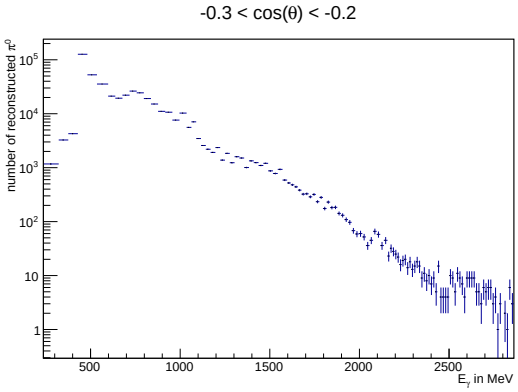

Figure 5.4: Number of reconstructed π^0 as a function of incident photon energy in the angular range between $\cos(\theta) = -0.3$ and $\cos(\theta) = -0.2$.

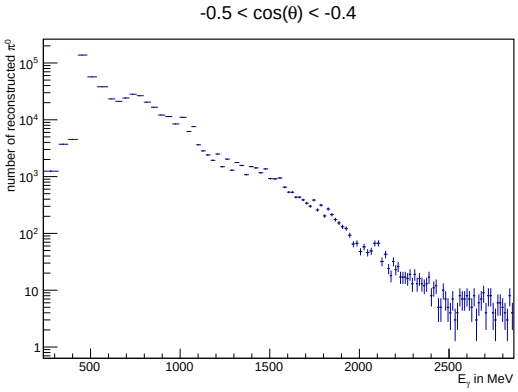

Figure 5.5: Number of reconstructed π^0 as a function of incident photon energy in the angular range between $\cos(\theta) = -0.5$ and $\cos(\theta) = -0.4$.

to be detected, but can be found in the missing mass spectrum. The missing mass corresponds to the invariant mass of the full system $m^2_{miss} = (E_{in} + E_{out})^2 - (p_{in} + p_{out})^2$. If there is a particle missing in the reconstruction, a peak will show in the spectrum. Fig. 5.2 shows this spectrum versus the two photon invariant mass spectrum. A peak is visible at the π^0 mass in the invariant mass spectrum and at the proton mass in the missing mass spectrum. By selecting only those events where the missing mass is within three σ of the peak around the proton mass, background can be reduced. The second constraint is co-planarity. In their rest frame the angle between π^0 and proton must be 180° (Fig. 5.3). Again, by cutting on the events within three σ of the peak around 180° in θ and ϕ the background can be reduced. The second data set in Fig. 5.1 (green) shows the two photon invariant mass spectrum after these cuts being applied. The peak at the π^0 mass was only a little bump before, but is now clearly visible. Furthermore, a second peak appeared in the spectrum, which corresponds to the η. Note that the plot has a logarithmic scale, the remaining background is negligible for this analysis. The π^0 are selected by cutting on four σ of the peak around the π^0 mass. Up to this point the analysis was independent of the angle at which the π^0 was detected. From here on, the angular range in θ_{cms} is divided in 20 bins with a width of $0.1 = \cos(\theta_{cms})$. The selected π^0 are then sorted in the corresponding bin and plotted as a function of incident photon energy. This is shown for a selection of bins in Fig. 5.4 and Fig. 5.5. For this work only angles covered by the BGO-ball are regarded to avoid extrapolation in unmeasured regions. These reconstructed π^0, however, are not all π^0 that were produced at the target, but only those detected.

5.1.2 Detection Efficiency

To get the full number of produced π^0 the detection efficiency has to be determined. This is done in simulation. The advantage of simulation is, that the total number of π^0 is known. The simulated data is then analysed in the same way as the real data. The detection efficiency is determined in the same angular bins that were used for the reconstruction of the π^0. The division of the number of reconstructed π^0 by the total number gives the energy dependent detection efficiency for each bin. It is depicted for the same bins as the spectrum of the π^0 in Fig. 5.6 and Fig. 5.7. The acceptance shows a large energy dependence, with a peak around 700 MeV and a decrease towards the edges of the spectrum. The alternating up-down structure is probably a binning effect. To get the total number of real π^0 the spectrum of reconstructed π^0 is divided by the detection efficiency.

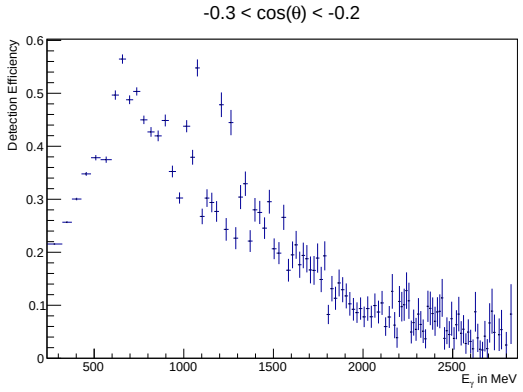

Figure 5.6: Detector acceptance determined from simulation as a function of incident photon energy.

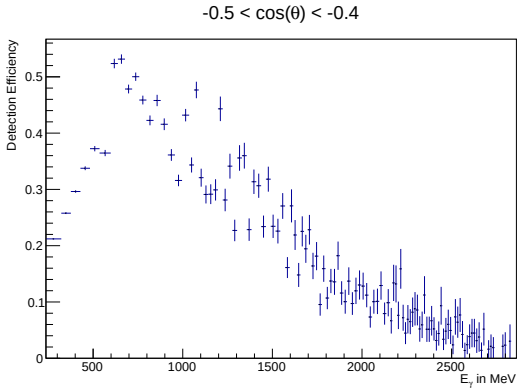

Figure 5.7: Detector acceptance determined from simulation as a function of incident photon energy.

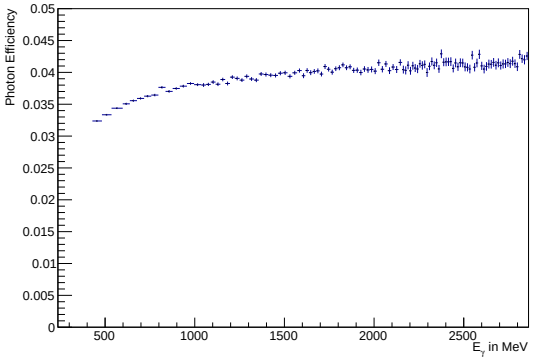

Figure 5.8: Photon efficiency determined from the full set of calibration runs of the October/November data taking period. At least two out of three FluMo scintillators were required.

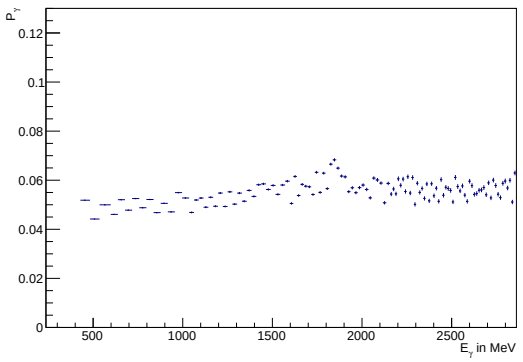

Figure 5.9: Tagging efficiency determined from the full set of data taking runs of the October/November data taking period and the photon efficiency shown in Fig. 5.8.

5.1.3 Photon Flux

The other important part is of course the photon flux. The photon efficiency has already been determined in chapter 3, the method to determine the tagging efficiency has been explained in chapter 4.1. This now needs to be applied to the full data taking period. To get an average photon efficiency all calibration runs are added and the photon efficiency is determined from the summed data. This is only possible since the photon efficiency was proven to be stable over the entire time. The result is shown in Fig. 5.8. Similarly the data taking runs are added and the tagging efficiency is obtained from this sum and the averaged photon efficiency. This averaged tagging efficiency is depicted in Fig. 5.9. An up-down structure, that was not visible with the less statistic of a single run can now be seen. Reason for this is probably a shift in the timing of the tagger channels. The systematic error caused by this structure is estimated to 2%. The "peak" around 1 800 MeV is caused by the linear polarisation of the photons.
From this now the absolute photon flux can be determined. As explained before, the Tagger scalers count the electron flux at the Tagger. Thus by dividing the Tagger scalers by the tagging efficiency the flux at the target can be obtained, it is shown in Fig. 5.10. While the Tagger TDCs count coincident hits in three Tagger scintillators once, the Tagger scalers count them as two double coincidences. This causes

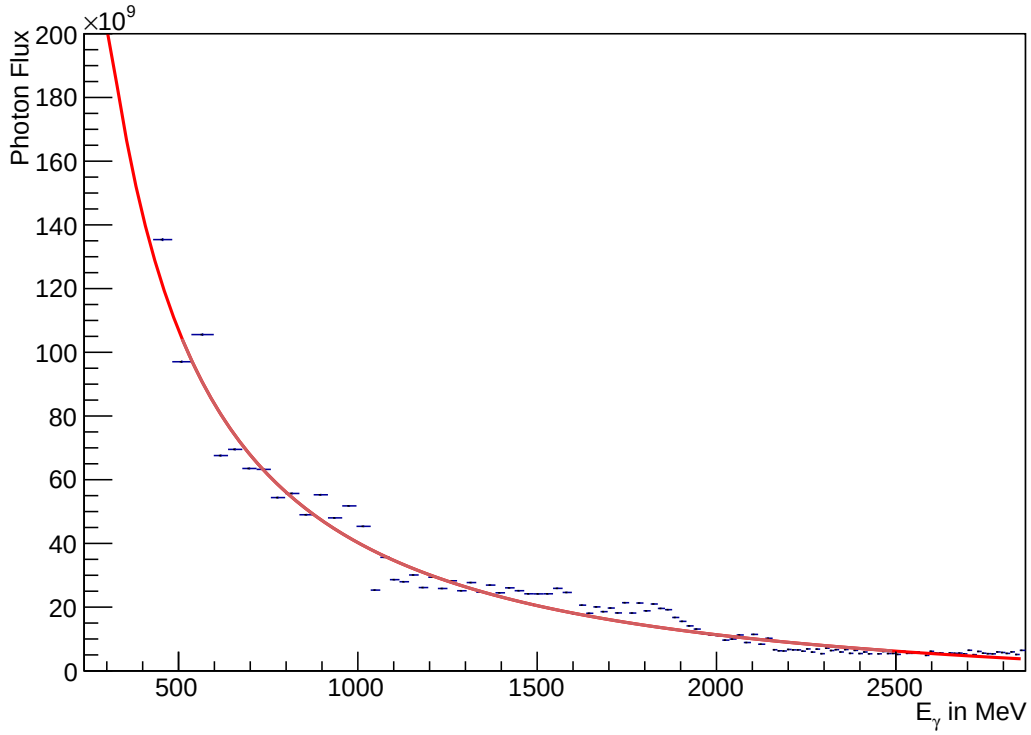

Figure 5.10: Photon flux determined from the Tagger scalers of the entire October/November data taking period and the tagging efficiency shown in Fig. 5.9. The red line is proportional to $\frac{1}{E_\gamma} \ln \frac{1}{E_\gamma}$.

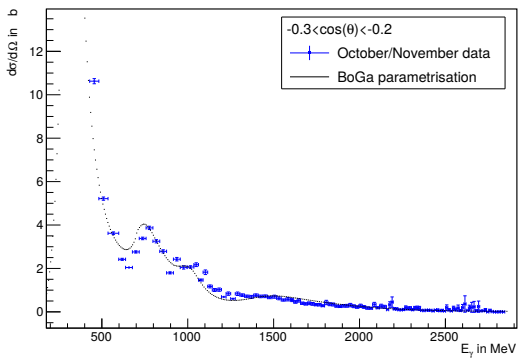

Figure 5.11: $\pi^0 p$ cross section in the angular range from $\cos(\theta) = -0.3$ to $\cos(\theta) = -0.2$.

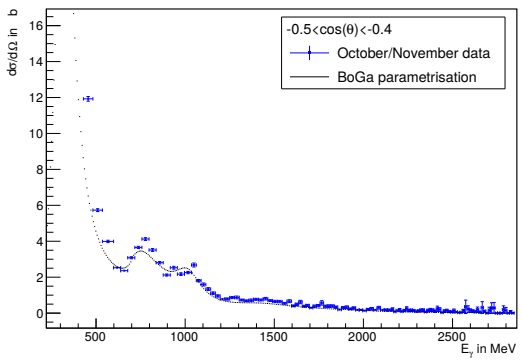

Figure 5.12: $\pi^0 p$ cross section in the angular range from $\cos(\theta) = -0.5$ to $\cos(\theta) = -0.4$.

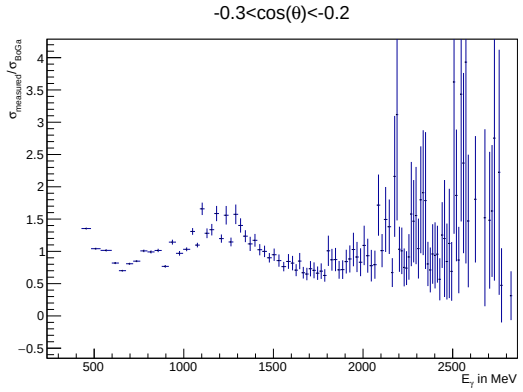

Figure 5.13: Ratio between experimental results and BoGa parametrisation in the angular range from $\cos(\theta) = -0.3$ to $\cos(\theta) = -0.2$.

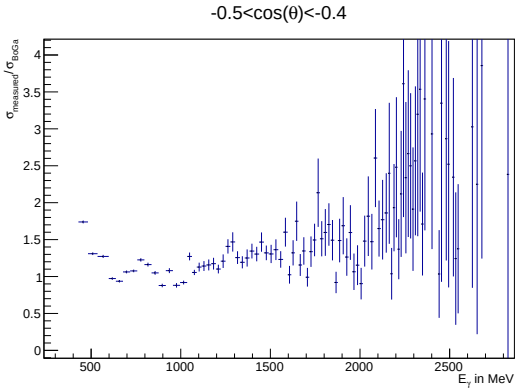

Figure 5.14: Ratio between experimental results and BoGa parametrisation in the angular range from $\cos(\theta) = -0.5$ to $\cos(\theta) = -0.4$.

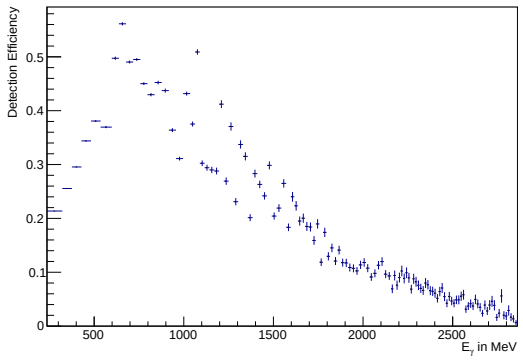

Figure 5.15: $\pi^0 p$ detection efficiency in the angular range from $\cos(\theta) = -0.5$ to $\cos(\theta) = 0.5$.

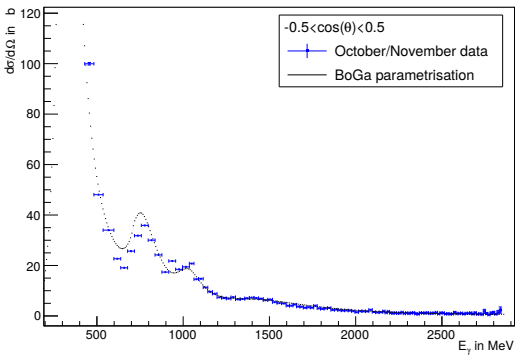

Figure 5.16: $\pi^0 p$ cross section in the angular range from $\cos(\theta) = -0.5$ to $\cos(\theta) = 0.5$.

an estimated systematic error of 5% on the obtained photon flux. The photon flux follows a $\frac{1}{E_\gamma} \ln \frac{1}{E_\gamma}$ dependence, indicated by the red line. The steps at 1 500 MeV and 1 800 MeV are like the peak in the tagging efficiency caused by linear polarisation of the photons.

5.2 Results

Finally all parts are put together. In Fig. 5.11 and Fig. 5.12 the resulting cross section is shown. The black dots are the parametrisation of the Bonn-Gatchina partial wave analysis [16]. The blue data points are the results of this work. The October/November data was analysed as described above, following Eqn. 5.1. In Fig. 5.13 and Fig. 5.14 the division of the result of this work and the BoGa-parametrisation is plotted.
Generally the data are in good agreement. In different angular bins different energy ranges fit better. This is probably caused by migration to neighbouring bins. To avoid this, the data is integrated over the angular range from $\cos(\theta_{cms}) = -0.5$ to $\cos(\theta_{cms}) = 0.5$ and the analysis is repeated. The result is shown in Fig. 5.15 to Fig. 5.17. The data are now in even better agreement. Certainly the analysis could be improved for even better results. Here the cross section is not the actual topic, but only used as a check

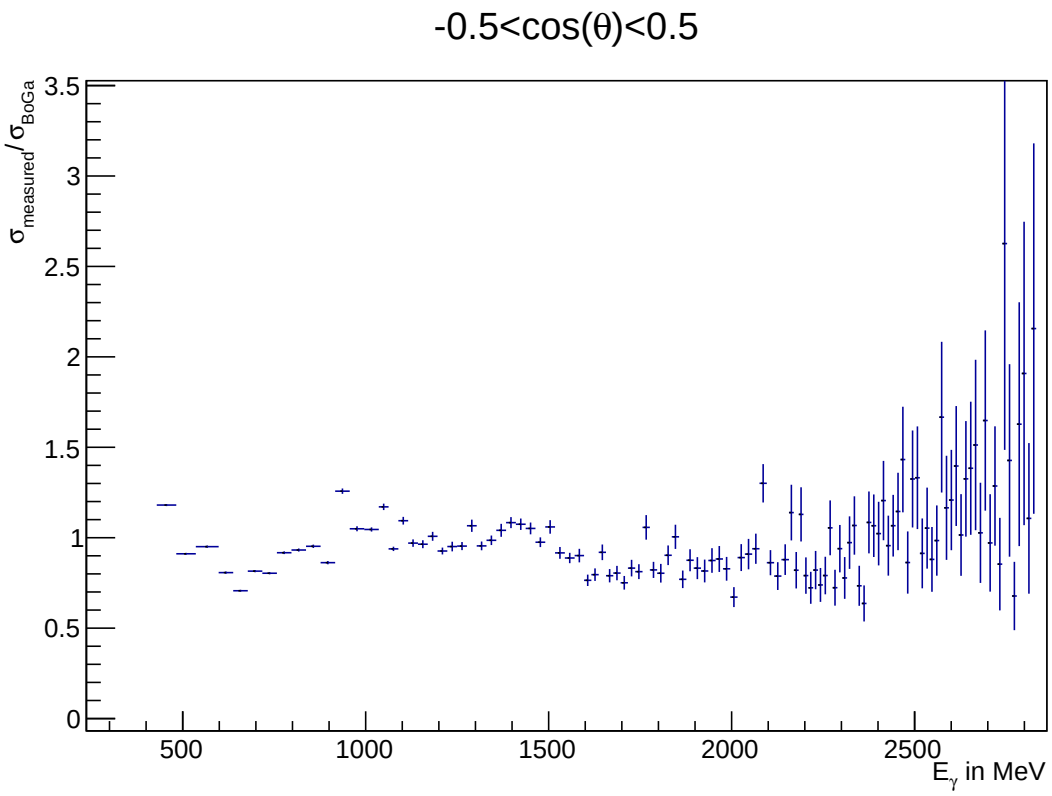

Figure 5.17: Tagging efficiency determined from the full set of data taking runs of the October/November data taking period and the photon efficiency shown in Fig. 5.8.

on the photon flux. Therefore a more detailed analysis would go beyond this thesis. As an upper limit for the systematic error of the photon flux, the difference to one is determined. With a value of 9% the error is much smaller than the difference to simulation with more than a factor of four. This result shows, that within few percent the flux determination works well. It must thus be concluded, that the discrepancy between simulation and experimental data lies in simulation.

CHAPTER 6

Summary and Conclusion

The BGO-OD experiment uses a tagged bremsstrahlung photon beam for photo-production of mesons off nucleons. An important constraint to understand these processes is the measurement of cross sections, prerequisite of which is the knowledge of the absolute photon flux. The aim of this thesis was to measure the absolute photon flux.

The photon flux is determined using the Tagger and a combination of a total absorbing Cerenkov detector (GIM) with a scintillator detector (FluMo), the latter measuring only a fraction of the photon flux. The Tagger determines the initial photon flux, GIM and FluMo are used to measure the collimated photon flux available at the target. While the GIM can measure the absolute photon flux directly, it is limited by rate and radiation damage. The FluMo only measures part of the flux, but up to very high rates. The GIM is used to calibrate the FluMo, which then provides in-situ measurements of the photon flux. Since the FluMo only measures part of the flux, this fraction needs to be known to determine the full flux. This fraction is called photon efficiency and must not be mistaken for the detection efficiency of the scintillators. The detection efficiency depends on thresholds and can change with rate. The photon efficiency however can be considered stable.
An improved method of determining the photon flux was introduced and a hardware upgrade of the FluMo was implemented. Two additional scintillators were added to the original three. This allows now to require only a subset of detectors to give a hit and therefore be less dependent on the individual detection efficiencies. It was shown that already with the old setup, a selection of two out of three scintillators gives much more stable results for the photon efficiency than requiring all three.
The fraction of the photon flux available at the target divided by to the initial photon flux is called tagging efficiency, and it represents the most essential quantity to determine the photon flux. In this work the tagging efficiency was determined from experimental data and simulation, which were found to disagree to a large extent. The simulated tagging efficiency is more than four times larger than the results from real data. The possibility of a misaligned collimator was analysed. A dedicated measurement indeed revealed a collimator misalignment of several mm with respect to the real beam. Even after correction real data and simulation still disagreed. The discrepancy between simulation and experimental data could be explained using different parameters in the simulation. In particular, a beam divergence three times larger than assumed brings the simulation in good agreement with the measurements.
As a cross check, the well known cross section $\gamma p \rightarrow \pi^0 p$ was extracted and compared to the results of the Bonn-Gatchina partial wave analysis. The results are in good agreement. The difference is of the order of few percent and thus much smaller than the difference between simulated and real tagging efficiency. It must therefore be concluded, that the tagging efficiency was determined correctly, and the

reason for the discrepancy between simulation and experimental data lies in simulation.
From the comparison of the measured cross section with the BoGa parametrisation an upper limit for the systematic error of 9% can be estimated for the flux determination. This can be improved using more data for the $\pi^0 p$ analysis. The uncertainty of the flux measurement itself is estimated to 5.7%

Bibliography

[1] B. Povh, *Teilchen und Kerne*, Springer, 2014 (cit. on p. 1).

[2] *Electron Stretcher Accelerator (ELSA) Homepage*, 2016,
URL: http://www-elsa.physik.uni-bonn.de/index_en.html (cit. on p. 4).

[3] B. Leibrock, *Erstinbetriebnahme der Vieldrahtproportionalkammer des BGO-OD Experiments*, Bachelor thesis, 2014 (cit. on p. 4).

[4] S. Böse, *Aufbau und Test eines neuen Szintillationsfaser-Detektors für das neue Vorwärtsspektrometer an ELSA*,
Dissertation: Physikalisches Institut, Rheinische Friedrich-Willhelms-Universität Bonn, 2015 (cit. on p. 4).

[5] T. Schwan, *Test und Inbetriebnahme der Driftkammern für das BGO-OD-Spektrometer*, Diploma thesis, 2010 (cit. on p. 4).

[6] P. Meiß, *The Time of Flight Spectrometer of the BGO-OD Experiment*, Diploma thesis, 2013 (cit. on p. 4).

[7] G. Scheluchin, *Meson photoproduction on the proton using the BGO-OD detector complemented by a new Scintillating Ring (SciRi)*, Master thesis, 2015 (cit. on p. 4).

[8] A. Bella, *Linearly polarised photons at the BGO-OD experiment at ELSA*,
Dissertation: Physikalisches Institut, Rheinische Friedrich-Willhelms-Universität Bonn, 2016 (cit. on p. 6).

[9] F. Messi, *The tagging system of the BGO-OD experiment*,
Dissertation: Physikalisches Institut, Rheinische Friedrich-Willhelms-Universität Bonn, 2015 (cit. on p. 6).

[10] P. B. Otte,
Erste Messung der π^0-Photoproduktion an transversal polarisierten Protonen nahe der Schwelle,
Dissertation: Johannes Gutenberg-Universität Mainz, 2015 (cit. on p. 7).

[11] T. Zimmermann, *Photon Flux Monitor for the BGO-OD Experiment*, Diploma thesis, 2012 (cit. on p. 8).

[12] D. Elsner, *Untersuchung kleiner Partialwellenbeiträge in der Nähe dominierender Resonanzzustände des Protons mit linear polarisierten Photonen*,
Dissertation: Physikalisches Institut, Rheinische Friedrich-Willhelms-Universität Bonn, 2007 (cit. on p. 18).

[13] *Particle Physics Booklet*, Particle Data Group, 2012 (cit. on pp. 18, 28).

[14] L. D. Landau and E. M. Lifschitz,
Course of theoretical physics, Volume 4 Part 1, Relativistic Quantum Theory,
Pergamon Press, 1971 (cit. on p. 19).

[15] S. Zander,
Strahldiagnos mit Synchrotronlichtmonitoren an der Elektronen-Stretcher-Anlage ELSA,
Dissertation: Physikalisches Institut, Rheinische Friedrich-Willhelms-Universität Bonn, 2013
(cit. on p. 25).

[16] *Bonn-Gatchina partial wave analysis*, 2016,
URL: http://pwa.hiskp.uni-bonn.de/BG2014_02_obs_int.html (cit. on p. 32).

APPENDIX A

Appendix

A.1 $\pi^0 p$ cross section

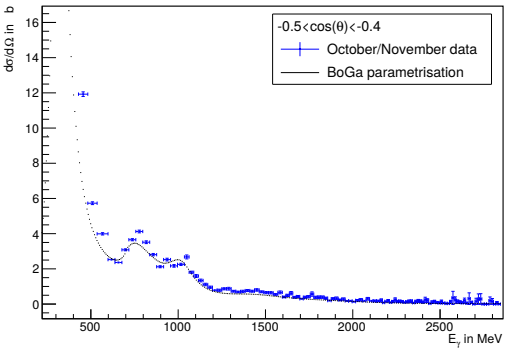

Figure A.1

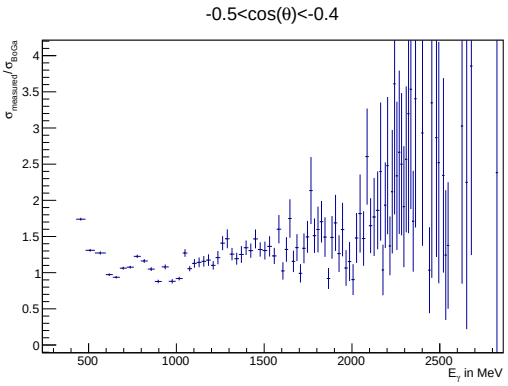

Figure A.2

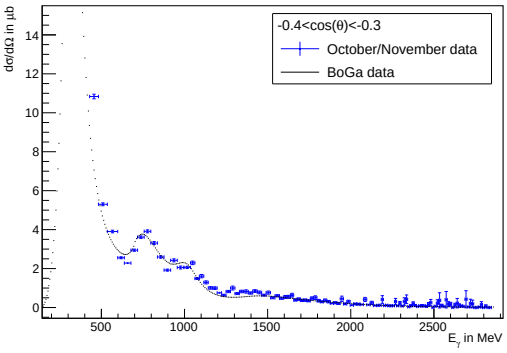

Figure A.3

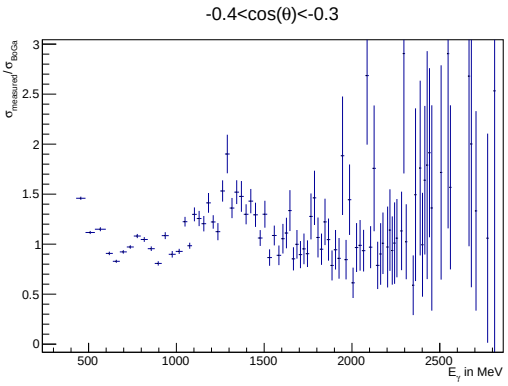

Figure A.4

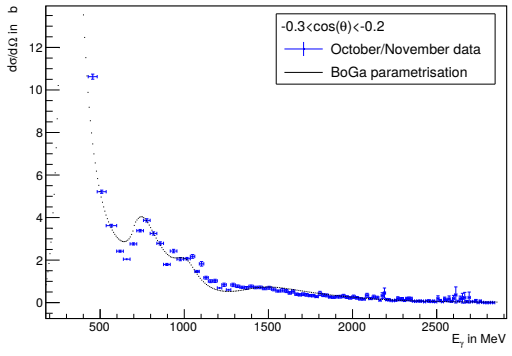

Figure A.5

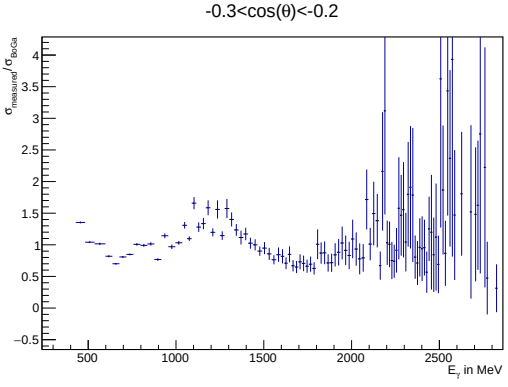

Figure A.6

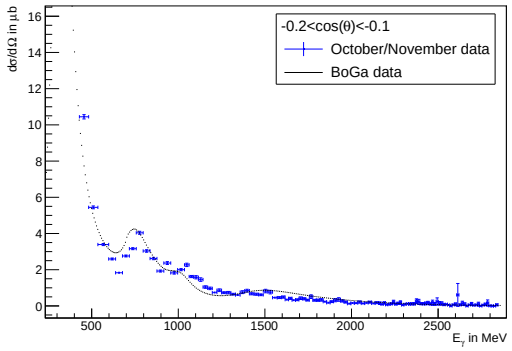

Figure A.7

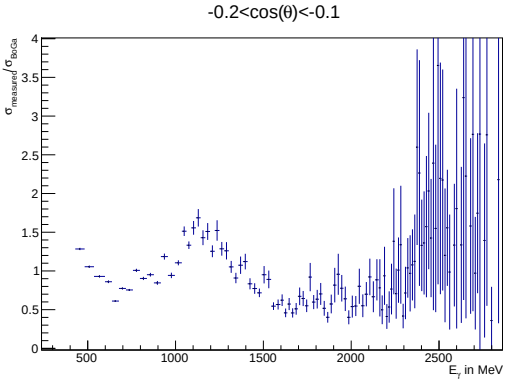

Figure A.8

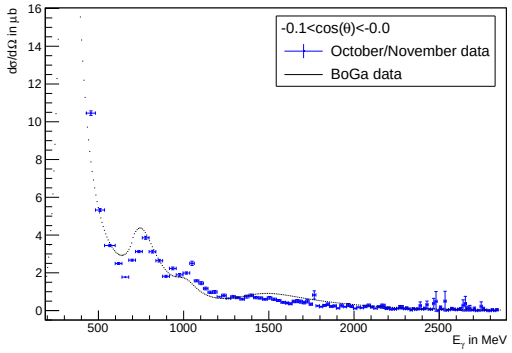

Figure A.9

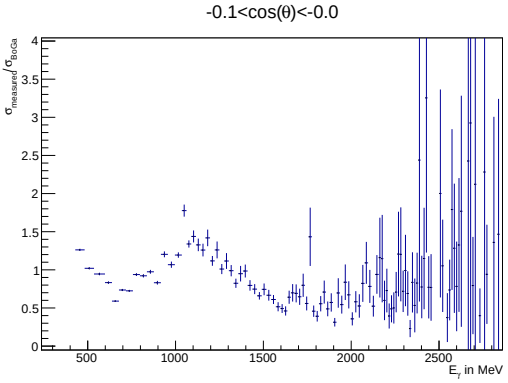

Figure A.10

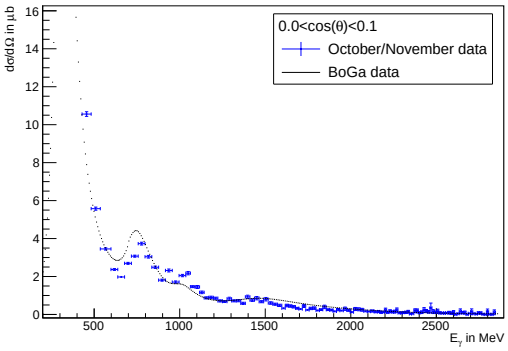

Figure A.11

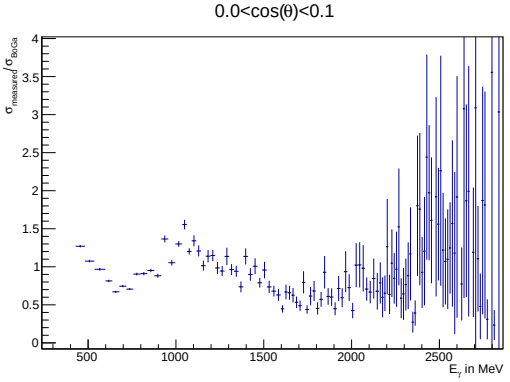

Figure A.12

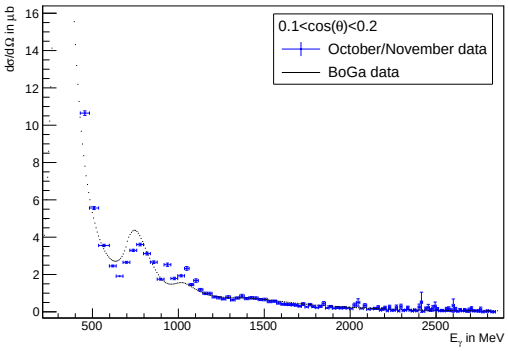

Figure A.13

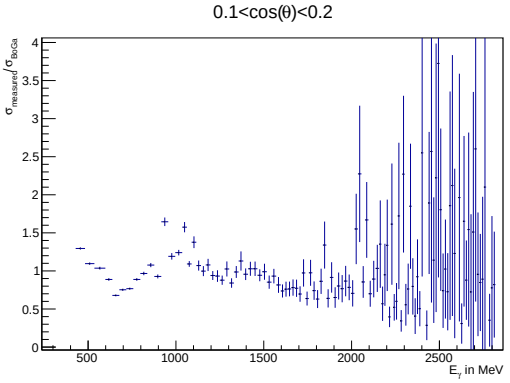

Figure A.14

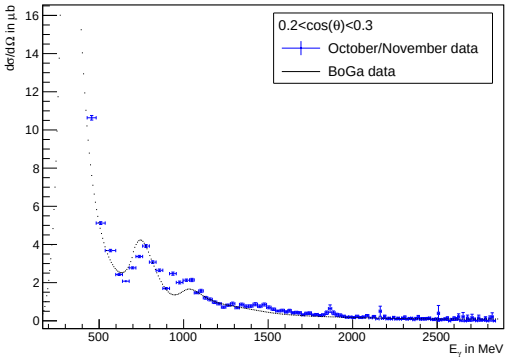

Figure A.15

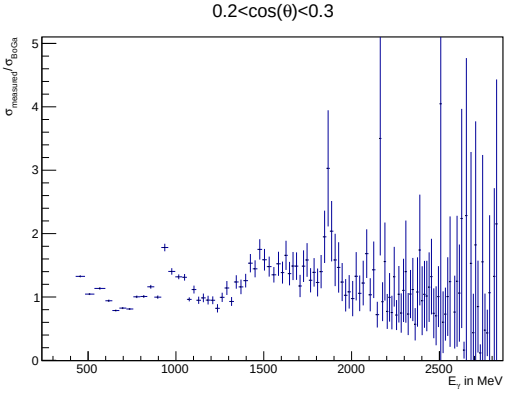

Figure A.16

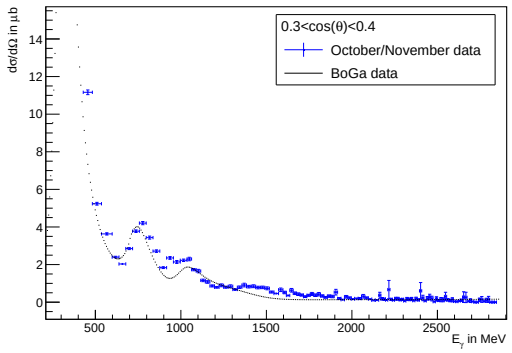

Figure A.17

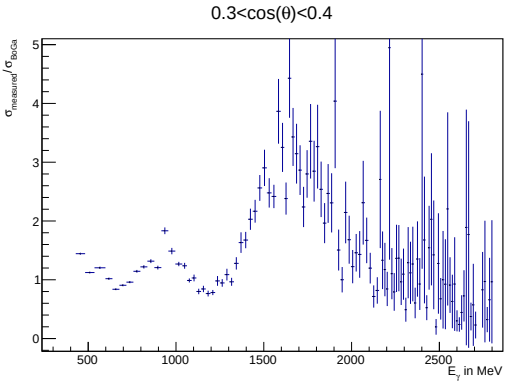

Figure A.18

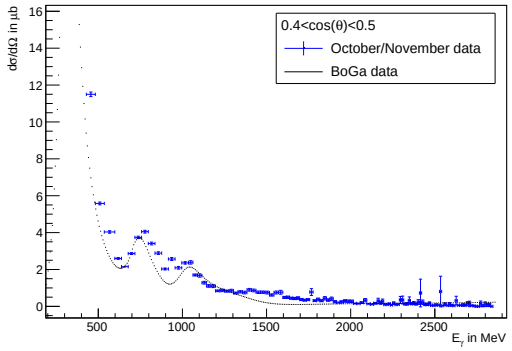

Figure A.19

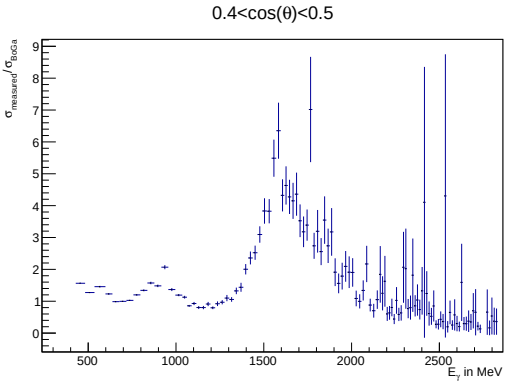

Figure A.20

List of Figures

2.1 Overview of ELSA. The beam is produced in the lower left corner at the LinAcs, continues through booster synchrotron and stretcher ring to the experiments. The experimental areas are shown in the upper left corner. 3
2.2 Overview of the BGO-OD experiment. The electron beam enters from the right and is converted to a photon beam which is incident upon a target in the center of the BGO-calorimeter. On the left side the forward spectrometer and the photon flux monitoring system are displayed. 5
2.3 Feynman-diagrams of an electron producing a bremsstrahlung-photon on a nucleon. . . 5
2.4 Overview of the tagging system. The beam enters from the left. The scintillators are shown in the lower right corner. Even further right the beam dump is visible. 6
2.5 Design of a single FluMo. The scintillator on the left is placed in the beam. 7
2.6 Schematic view of the original setup with three scintillators and a converter 8
2.7 Schematic view of the improved setup with five scintillators 8

3.1 TDC spectrum with the meantime of all coincidences where at least 2 out of 3 FluMos were required. Shaded blue is the prompt peak that is used to determine the photon efficiency. The dip on the left side of the peak occurs due to dead time of the detectors. 9
3.2 The plot depicts the time difference of two detectors respectively. On the x-axis the time difference of FluMo and Tagger, on the y-axis the time difference of GIM and Tagger is shown. The visible lines correspond to true coincidences of two detectors, at the intersection all three detectors coincide. The background consists of uncorrelated coincidences. The boxes indicate the boxes for the background subtraction. 10
3.3 Photon efficiency as a function of energy. A background correction has been applied to the blue data. The comparison to the uncorrected photon efficiency (red data) shows a systematic increase. 11
3.4 The photon efficiency is determined from Tagger-GIM-FluMo coincidences divided by Tagger-GIM coincidences. 11
3.5 In the plot the maximum value of the photon efficiency, determined from a linear fit is shown for several data sets over the full data taking period in November 2015. For the blue data at least two out of three scintillators were required, for the red data all three. . 12
3.6 The plot shows the efficiencies of the original three scintillators for all runs of the data taking period in November 2015. The instability is clearly visible. Especially the second scintillator changed a lot after threshold setting. 13
3.7 In the plot the maximum value of the photon efficiency, determined from a linear fit is shown for several data sets with the updated FluMo setup with five scintillators. The efficiency is plotted as a function of the Tagger rate for all numbers of required coincidences. 14

4.1 TDC time spectrum of the Tagger. The central peak contains triggered events. To avoid artifacts from trigger requirements not this peak, but the sidebands shaded in blue are used for determining the tagging efficiency. . . . 15
4.2 Time difference of Tagger and FluMo. The central peak contains true coincidences and background of uncorrelated coincidences. This background is determined with boxes (shaded in blue) and subtracted. . . . 15
4.3 The tagging efficiency is determined from Tagger-FluMo coincidences divided by Tagger hits and photon efficiency. . . . 16
4.4 Tagging efficiency determined from run 31917 as a function of photon energy. Shown in blue is the tagging efficiency determined from at least two scintillators, in red the tagging efficiency requiring all three. . . . 17
4.5 Tagging efficiency for a selection of runs over the entire data taking period. Shown in blue is the tagging efficiency determined from at least two scintillators, in red the tagging efficiency requiring all three. The blue data is shifted to the left so both data sets are visible. 17
4.6 Collimation of the photon beam at the BGO-OD experiment. The electron beam coming from the left is converted to photons at the radiator. At a distance of 3.6 m a collimator is placed. The sketch is not to scale. . . . 18
4.7 Simulated and analytically determined tagging efficiency for different beam energies. The analysis is done for an ideal beam where beam spot and beam divergence are zero. 19
4.8 Simulated tagging efficiency for a beam energy of 3 200 MeV. Here a realistic beam size and beam divergence are included in the simulation. . . . 20
4.9 Simulation of the tagging efficiency for different collimator positions. The collimator is either shifted in x or y, or rotated around θ. . . . 21
4.10 Beam spot without first collimator. . . . 23
4.11 projection on the x-axis of the beam spot without first collimator. . . . 23
4.12 Beam spot with badly aligned first collimator. . . . 23
4.13 projection on the x-axis of the beam spot with badly aligned first collimator. . . . 23
4.14 Beam spot with well aligned first collimator. . . . 23
4.15 projection on the x-axis of the beam spot with well aligned first collimator. . . . 23
4.16 Tagging efficiency from experimental data (blue) and simulation (red) without collimator. For the simulated green data the beam divergence was multiplied with a factor three to fit the experimental data. . . . 24
4.17 Tagging efficiency from experimental data with badly aligned collimator. . . . 24
4.18 Tagging efficiency from experimental data (blue) and simulation (red) with well aligned collimator. For the simulated green data the beam divergence was multiplied with a factor three to fit the experimental data. . . . 24

5.1 Number of photon pairs as a function of their invariant mass. In blue the full data set is shown, the green set shows the data after several selective cuts have been applied to reduce background. . . . 27
5.2 Spectrum of the missing mass versus two photon invariant mass. A peak is visible at the π^0 mass in the invariant mass spectrum and at the proton mass in the missing mass spectrum. . . . 28
5.3 Angular distribution between π^0 and p-candidates in ϕ and θ. The box indicates the three σ width of the peak at 180° in θ and ϕ. . . . 28
5.4 Number of reconstructed π^0 as a function of incident photon energy in the angular range between $\cos(\theta) = -0.3$ and $\cos(\theta) = -0.2$. . . . 29

5.5 Number of reconstructed π^0 as a function of incident photon energy in the angular range between $\cos(\theta) = -0.5$ and $\cos(\theta) = -0.4$. 29
5.6 Detector acceptance determined from simulation as a function of incident photon energy. 30
5.7 Detector acceptance determined from simulation as a function of incident photon energy. 30
5.8 Photon efficiency determined from the full set of calibration runs of the October/November data taking period. At least two out of three FluMo scintillators were required. 30
5.9 Tagging efficiency determined from the full set of data taking runs of the October/November data taking period and the photon efficiency shown in Fig. 5.8. 30
5.10 Photon flux determined from the Tagger scalers of the entire October/November data taking period and the tagging efficiency shown in Fig. 5.9. The red line is proportional to $\frac{1}{E_\gamma} \ln \frac{1}{E_\gamma}$. 31
5.11 $\pi^0 p$ cross section in the angular range from $\cos(\theta) = -0.3$ to $\cos(\theta) = -0.2$. 31
5.12 $\pi^0 p$ cross section in the angular range from $\cos(\theta) = -0.5$ to $\cos(\theta) = -0.4$. 31
5.13 Ratio between experimental results and BoGa parametrisation in the angular range from $\cos(\theta) = -0.3$ to $\cos(\theta) = -0.2$. 32
5.14 Ratio between experimental results and BoGa parametrisation in the angular range from $\cos(\theta) = -0.5$ to $\cos(\theta) = -0.4$. 32
5.15 $\pi^0 p$ detection efficiency in the angular range from $\cos(\theta) = -0.5$ to $\cos(\theta) = 0.5$. 32
5.16 $\pi^0 p$ cross section in the angular range from $\cos(\theta) = -0.5$ to $\cos(\theta) = 0.5$. 32
5.17 Tagging efficiency determined from the full set of data taking runs of the October/November data taking period and the photon efficiency shown in Fig. 5.8. 33

A.1 39
A.2 39
A.3 39
A.4 39
A.5 40
A.6 40
A.7 40
A.8 40
A.9 40
A.10 40
A.11 41
A.12 41
A.13 41
A.14 41
A.15 41
A.16 41
A.17 42
A.18 42
A.19 42
A.20 42